



ATLAS CONF Note Draft

HIGG-2019-06

Version 1.0

Comments are due by: 15 March 2021

Supporting internal notes

Supporting Note: <https://cds.cern.ch/record/2703097>

Differential High- p_T $H \rightarrow b\bar{b}$ Production Studies in 13 TeV pp Collisions with the ATLAS Detector

This paper reports studies of Higgs boson production with sizeable transverse momentum decaying to a $b\bar{b}$ quark pair with the ATLAS detector. The analyzed data were recorded by the ATLAS detector in proton–proton collisions with a center-of-mass energy of $\sqrt{s} = 13$ TeV at the Large Hadron Collider between 2015–2018, corresponding to an integrated luminosity of 136 fb^{-1} . Higgs bosons decaying to $b\bar{b}$ are reconstructed as single large-radius jets and identified by the experimental signature of two b -hadron decays. The experimental techniques are validated in the same kinematic regime using the $Z \rightarrow b\bar{b}$ process. For Higgs boson production at transverse momenta above 450 GeV, the measured production cross section is $13 \pm 57(\text{stat.}) \pm 22(\text{syst.}) \pm 3(\text{theo.}) \text{ fb}$. The differential cross section 95% confidence interval limits in function of Higgs boson transverse momentum p_T^H obtained are $\sigma_H(300 < p_T^H < 450 \text{ GeV}) < 2.8 \text{ pb}$, $\sigma_H(450 < p_T^H < 650 \text{ GeV}) < 91 \text{ fb}$, $\sigma_H(p_T^H > 650 \text{ GeV}) < 40.5 \text{ fb}$, and $\sigma_H(p_T^H > 1 \text{ TeV}) < 10.3 \text{ fb}$. All results are in agreement with Standard Model predictions.

Analysis Team

[*email:* atlas-HIGG-2019-06-editors@cern.ch]

Marco Battaglia, Lydia Beresford, Federico Celli, Gabriel Facini, Francesco Maria
Follega, James Frost, Matthew Gignac, Cole Michael Helling, Joey Huston, Roberto
Iuppa, Eleanor Jones, Karol Krizka, Bill Murray, Jason Nielsen, Jose Gabriel Reyes
Rivera, Andrea Sciandra, Mige Stankaityte, Ahmed Tarek Abouelfadl Mohamed, Rafael
Teixeira de Lima

Editorial Board

[*email:* atlas-HIGG-2019-06-editorial-board@cern.ch]

Gustaaf Brooijmans (chair)
Pierre-Antoine Delsart
Paolo Francavilla

Language editor: language editor contact



ATLAS CONF Note

HIGG-2019-06

March 8, 2021



Draft version 1.0

Differential High- p_T $H \rightarrow b\bar{b}$ Production Studies in 13 TeV pp Collisions with the ATLAS Detector

The ATLAS Collaboration

This paper reports studies of Higgs boson production with sizeable transverse momentum decaying to a $b\bar{b}$ quark pair with the ATLAS detector. The analyzed data were recorded by the ATLAS detector in proton–proton collisions with a center-of-mass energy of $\sqrt{s} = 13$ TeV at the Large Hadron Collider between 2015–2018, corresponding to an integrated luminosity of 136 fb^{-1} . Higgs bosons decaying to $b\bar{b}$ are reconstructed as single large-radius jets and identified by the experimental signature of two b -hadron decays. The experimental techniques are validated in the same kinematic regime using the $Z \rightarrow b\bar{b}$ process. For Higgs boson production at transverse momenta above 450 GeV, the measured production cross section is $13 \pm 57(\text{stat.}) \pm 22(\text{syst.}) \pm 3(\text{theo.}) \text{ fb}$. The differential cross section 95% confidence interval limits in function of Higgs boson transverse momentum p_T^H obtained are $\sigma_H(300 < p_T^H < 450 \text{ GeV}) < 2.8 \text{ pb}$, $\sigma_H(450 < p_T^H < 650 \text{ GeV}) < 91 \text{ fb}$, $\sigma_H(p_T^H > 650 \text{ GeV}) < 40.5 \text{ fb}$, and $\sigma_H(p_T^H > 1 \text{ TeV}) < 10.3 \text{ fb}$. All results are in agreement with Standard Model predictions.

Contents

1	Introduction	2
2	ATLAS detector	4
3	Data and simulated sample	4
4	Object selection	5
4.1	Object Reconstruction	6
4.2	Analysis Object Definitions	7
4.3	Experimental Systematic Uncertainties	7
5	Event categorization	8
5.1	Signal and Validation Regions	8
5.2	$t\bar{t}$ Control Region	9
6	Higgs boson modeling	9
7	Background process modeling	10
7.1	Top-quark pair production	11
7.2	V+jets production	11
7.3	Multijet production	14
8	Statistical analysis	16
9	Results	17
9.1	Inclusive region	18
9.2	Fiducial $p_T^H > 450$ GeV and $p_T^H > 1$ TeV regions	19
9.3	Differential regions	21
10	Conclusions	24
Appendix		25

1 Introduction

The characterization of the Higgs sector has steadily improved since the Higgs boson (H) discovery [1, 2] using proton–proton (pp) collision data produced by the Large Hadron Collider (LHC) at CERN. Five production modes: gluon–gluon fusion (ggF), vector–boson fusion (VBF), associated production with a weak vector boson (WH or ZH , collectively VH), and associated production with a top–antitop pair ($t\bar{t}H$) and five decay modes: $H \rightarrow \gamma\gamma, ZZ^*, WW^*, \tau\tau, b\bar{b}$ have been observed [3, 4]. Inclusive cross-section measurements have evolved to differential measurements and measurements in kinematic regions defined within the simplified template cross-section framework (STXS) [5–7]. All results agree with the Standard Model (SM) predictions, but sizeable regions of the Higgs sector remain unexplored. In one such region, where the Higgs boson transverse momentum, p_T^H , reaches the TeV scale, the cross section hierarchy is

very different from the inclusive cross section where ggF is nearly 90% of the total. At the TeV scale, ggF, VH , and the sum of the VBF and $t\bar{t}H$ production cross sections are all roughly equal.

The leading effects of many beyond the SM (BSM) scenarios, such as those encapsulated in effective field theories (EFTs), can be parametrized through effective operators suppressed by the new physics scale Λ . The most energetic parton-level interactions at the LHC allow access to regions where some operators' effects are enhanced by powers of E/Λ . Here, measurements with an extended energy reach outperform precise low-energy measurements in new physics sensitivity as the signal-to-background ratio increases with p_T . The differential cross section as a function of the Higgs boson transverse momentum exemplifies this potential as it is sensitive to BSM contributions that mainly impact high- p_T Higgs production [8–12]. For example, the ggF process is sensitive to the structure of quasi point-like couplings within the loop nature of the effective ggH coupling. Using the $H \rightarrow b\bar{b}$ decay, which exhibits the largest branching fraction, mitigates the impact of the reduced absolute cross section in the high- p_T regime.

This paper reports the first ATLAS studies of high- p_T Higgs bosons decaying to a $b\bar{b}$ pair where no restrictions are applied to select a particular Higgs boson production mode and the production yield is determined in different p_T^H regions. The fiducial cross section is measured for $p_T^H > 450$ GeV, $p_T^H > 1$ TeV and within three p_T^H bin intervals: 250–450 GeV, 450–650 GeV, and above 650 GeV. The dataset used corresponds to 136 fb⁻¹ of proton–proton (pp) collisions at $\sqrt{s} = 13$ TeV collected with the ATLAS detector [13] using jet-based trigger requirements during Run 2 (2015–2018) of the LHC. The CMS Collaboration measured the ggF production mode signal strength to be $\mu_H = 3.7^{+1.6}_{-1.5}$ in the $H \rightarrow b\bar{b}$ decay mode and presented differential cross sections using events within the high- p_T^H regime [14].

Higgs boson candidates with large Lorentz boosts are reconstructed as single large-radius jets having a mass compatible with 125 GeV. To populate the signal region, events must have at least two jets, where one exceeds 450 GeV, to ensure a fully efficient trigger response, and at least one contains evidence of two b -hadron decays. Both the leading and subleading jet in the event are considered in the identification of Higgs boson candidates: including the subleading jet increases the sensitivity for $p_T^H > 450$ GeV by 11% and permits a fiducial cross-section measurement down to $p_T^H = 300$ GeV, overlapping with measurements in other decay channels. For a Higgs boson mass (m_H) of 125 GeV, the SM predicts ggF-produced events to be the largest contribution reconstructed near m_H in all but one fiducial region considered. However, $t\bar{t}H$ -produced events are nearly 40% of the total in the lowest p_T region. VH -produced events account for around 25% of all Higgs boson events in the subleading jet category. VBF-produced events consistently contribute for over 15% of the total yield.

The dominant background process is multijet events and exhibits a monotonically decreasing jet mass distribution. Hadronically decaying vector bosons, produced in association with jets (V +jets) and events with top-quarks ($t\bar{t}$) populate the mass regions below and above m_H , respectively, as shown in Figure 1. The Z and H resonance structures are distinct from the smoothly falling multijet background while the top-quark resonance spreads over a large portion of the high-mass region. Therefore, the signal extraction uses the reconstructed jet mass distribution as a discriminant and an analytic function is used to model the multijet background. The acceptance of Higgs boson, V +jets, and $t\bar{t}$ events are estimated from simulation. The Z normalization is determined directly from the signal region data, while a dedicated control region is used to determine the $t\bar{t}$ yield. A validation region is used to study the parameterization of the multijet model and V +jets events. A binned maximum-likelihood fit, referred to as the global likelihood fit, extracts the Higgs boson contribution in the signal region. Extracting the Z yield in the signal region with the same method provides a validation of the analysis techniques.

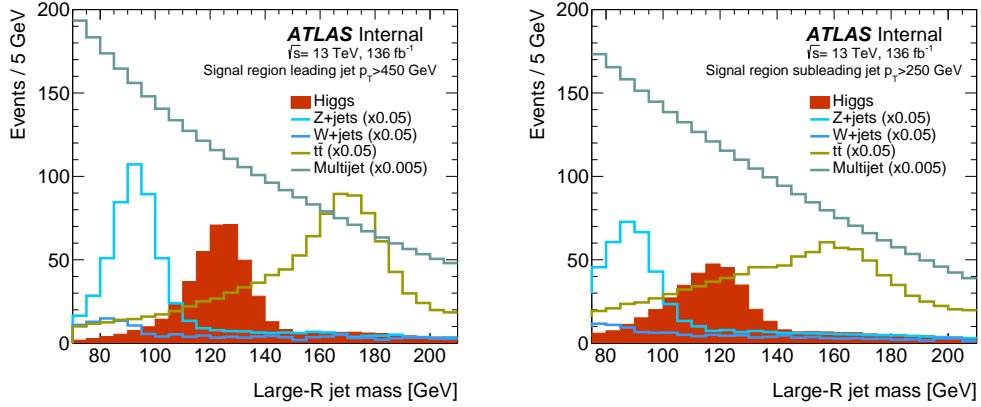


Figure 1: The H , Z , W , $t\bar{t}$ and multijet jet mass distributions for the signal region defined by the leading (SRL, left) and subleading (SRS, right) jets using the selection adopted in the analysis.

2 ATLAS detector

The ATLAS experiment [13] at the LHC is a multi-purpose particle detector with a forward-backward symmetric cylindrical geometry and a near 4π coverage in solid angle.¹ It consists of an inner tracking detector surrounded by a thin superconducting solenoid providing a 2 T axial magnetic field, electromagnetic and hadron calorimeters, and a muon spectrometer. The inner tracking detector covers the pseudorapidity range $|\eta| < 2.5$. It consists of silicon pixel, silicon microstrip, and transition radiation tracking detectors. Lead/liquid-argon (LAr) sampling calorimeters provide electromagnetic (EM) energy measurements with high granularity. A hadron (steel/scintillator-tile) calorimeter covers the central pseudorapidity range ($|\eta| < 1.7$). The forward regions are instrumented with LAr calorimeters for both EM and hadronic energy measurements up to $|\eta| = 4.9$. The muon spectrometer surrounds the calorimeters and is based on three large air-core toroidal superconducting magnets with eight coils each. The field integral of the toroids ranges between 2.0 and 6.0 T m across most of the detector. The muon spectrometer includes a system of precision tracking chambers and fast detectors for triggering. A two-level trigger system is used to select events. The first-level trigger is implemented in hardware and uses a subset of the detector information to reduce the accepted rate to at most 100 kHz. A software-based trigger further reduces the accepted event rate to 1 kHz on average.

3 Data and simulated sample

The data were collected with the ATLAS detector in pp collisions with a center-of-mass energy of 13 TeV during Run 2 (2015–2018) of the LHC. Events must satisfy a set of triggers requiring a reconstructed anti- k_t jet with radius parameter $R = 1.0$ [15] or a muon with $p_T > 50$ GeV. To adapt to different instantaneous luminosity profiles and the inclusion of pile-up suppressing techniques within the data acquisition system [16], the jet p_T and mass thresholds differ for each year of data taking. The trigger jet p_T

¹ ATLAS uses a right-handed coordinate system with its origin at the nominal interaction point (IP) in the center of the detector and the z -axis along the beam pipe. The x -axis points from the IP to the center of the LHC ring, and the y -axis points upwards. Cylindrical coordinates (r, ϕ) are used in the transverse plane, ϕ being the azimuthal angle around the z -axis. The pseudorapidity is defined in terms of the polar angle θ as $\eta = -\ln \tan(\theta/2)$. Angular distance is measured in units of $\Delta R \equiv \sqrt{(\Delta\eta)^2 + (\Delta\phi)^2}$.

threshold varies from 360 GeV to 420 GeV, and the trigger jet mass threshold is either not applied, 30 GeV, or 35 GeV. The total integrated luminosity is 136 fb^{-1} and 139 fb^{-1} for the jet- and muon-triggered data, respectively, with an uncertainty of 1.7% [17, 18].

Monte Carlo (MC) simulated events are used to model the resonant backgrounds (W + jets, Z + jets, and $t\bar{t}$) as well as four Higgs production processes: ggF, VBF, VH , and $t\bar{t}H$.

Higgs boson ggF production is simulated at next-to-leading-order (NLO) accuracy in QCD with finite mass effects by using the HJ-MiNLO [19–21] prescription with the POWHEG program [22–24] as discussed in Ref. [25]. NLO accuracy in QCD and electroweak (EW) effects is achieved for VBF, VH , and $t\bar{t}H$ production. The Higgs boson branching fractions are calculated with HDECAY [26–28] and PROPHECY4F [29–31]. The production cross sections used are compatible with those presented in Ref. [32] except for $t\bar{t}H$ production where an overall scale factor is applied to recover the difference.

V + jets production with hadronic decays is simulated with SHERPA to NLO QCD accuracy for 1 additional parton and LO QCD accuracy for up to 4 additional partons. Approximate NLO EW corrections are applied as a function of the generated vector boson momentum p_T^V . They have a sizeable impact on the differential production cross section decreasing the predicted yield by $\sim 10\%$ at p_T^V of 500 GeV and $\sim 20\%$ above 1 TeV. Calculations of next-to-next-to-leading-order (NNLO) QCD corrections to V + jets productions are available [33]. The NNLOJET group performed the calculation for $\sqrt{s} = 8 \text{ TeV}$ [34, 35] and has provided custom k-factors for the analysis fiducial region as a function p_T^V . They vary from 1.013 to 1.081.

The production of top-quark pairs, associated production of top quarks with W bosons (Wt), and single-top t - and s -channel production are modeled using the POWHEG-Box v2 [22–24, 36–39] generator at NLO in QCD. The diagram removal scheme [40] is used in Wt events to remove interference and overlap with $t\bar{t}$ production.

An analytic function models non-resonant multijet events while simulated events are available to study the method. Multijet production is generated using PYTHIA 8.230 [41] with leading-order matrix elements for dijet production and interfaced to a p_T ordered parton shower.

All simulated collision particles are processed with the ATLAS detector simulation [42] based on GEANT 4 [43]. Pile-up, multiple interactions in the same and neighboring bunch crossings, is modeled by overlaying simulated inelastic pp events generated with PYTHIA 8.186 [41] using the NNPDF2.3LO set of parton distribution functions (PDFs) [44] and the A3 tune [45] over the original hard-scattering event. For Higgs boson and $t\bar{t}$ production, the EVTGEN v1.2.0 program [46] models the decays of bottom and charm hadrons.

For each sample, Table 1 summarizes the MC generators, parton distribution functions, and underlying event tunes used as well as the order of perturbative QCD computations and EW corrections obtained for the cross section. For additional information, see Ref. [47] for V + jets events, Refs. [48–50] for $t\bar{t}$ events, and Ref. [51] for dijet events. Systematic uncertainties for process modeling are described in Section 7.

4 Object selection

For large Higgs boson boost, the event topology of $pp \rightarrow H(\rightarrow b\bar{b}) + j$ is characterised by two jets, one of which, due to the considerable Lorentz boost, contains the decay products of the two b -hadrons.

Table 1: The generators used for the simulation of the signal and background processes. Matrix element, parton shower and underlying event are abbreviated as ME, PS, and UE respectively. (*) PowHEG was configured to output events with Born k_T above 200 GeV using the *bornkmin* setting. (•) Corrections for NLO EW effects computed with HAWK [52, 53] are applied as a function of the generated Higgs boson transverse momentum. (◦) Corrections for NLO EW effects computed with SHERPA + OPENLOOPS 1 [54–56] are applied as a function of the generated Higgs boson transverse momentum and were provided by Ref. [32]. (†) SHERPA provides 1 additional parton at NLO order accuracy and up to 4 additional partons at LO in QCD and custom NNLO QCD corrections were provided by the NNLOJET group.

Process	ME generator	ME PDF	PS and Hadronisation	UE model tune	Cross-section order
Higgs Boson					
$gg \rightarrow H \rightarrow b\bar{b}$	PowHEG-Box v2 ^(*) [22–24]+ MiNLO [19–21]	NNPDF3.0NNLO [57]	PYTHIA 8.212 [41]	AZNLO [58]	NLO(QCD) + LO(EW)
$qq \rightarrow H \rightarrow q'q'b\bar{b}$	PowHEG-Box v2 [22–24, 59]	NNPDF3.0NLO [57]	PYTHIA 8.230	AZNLO	NLO(QCD) + NLO(EW) ^(•)
$qq \rightarrow WH$ $\rightarrow qq'b\bar{b}$ $\rightarrow \ell\nu b\bar{b}$	PowHEG-Box v2 + GoSAM [60] + MiNLO [61]	NNPDF3.0NLO	PYTHIA 8.240 PYTHIA 8.212	AZNLO	NNLO(QCD) + NLO(EW) ^(•)
$qq \rightarrow ZH$ $\rightarrow q\bar{q}b\bar{b}$ $\rightarrow \nu\nu b\bar{b}$ $\rightarrow \ell\ell b\bar{b}$	PowHEG-Box v2 + GoSAM+ MiNLO	NNPDF3.0NLO	PYTHIA 8.240 PYTHIA 8.212	AZNLO	NNLO(QCD)+ NLO(EW) ^(•)
$gg \rightarrow ZH$ $\rightarrow q\bar{q}b\bar{b}$ $\rightarrow \nu\nu b\bar{b}$ $\rightarrow \ell\ell b\bar{b}$	PowHEG-Box v2	NNPDF3.0NLO	PYTHIA 8.240 PYTHIA 8.212	AZNLO	LO + NLL(QCD)
$gg \rightarrow t\bar{t}H$ $t\bar{t} \rightarrow \text{all}$ $H \rightarrow \text{all}$	PowHEG-Box v2 [62]	NNPDF3.0NLO	PYTHIA 8.230	AZNLO	NLO(QCD) + NLO(EW) ^(◦)
Vector boson + jets					
$W \rightarrow qq$ $Z \rightarrow qq$	SHERPA 2.2.8 [55, 63, 64]	NNPDF3.0NNLO	SHERPA 2.2.8 [65, 66]	Default	NNLO(QCD) ^(†) [34, 35, 67] approx NLO(EW) [68, 69]
Top quark, mass set to 172.5 GeV					
$t\bar{t} \rightarrow \text{all}$	PowHEG-Box v2 [22–24, 36]	NNPDF3.0NLO	PYTHIA 8.230	A14 [70]	NNLO+NNLL [71]
$t \rightarrow Wb$	PowHEG-Box v2 [22–24, 37]	NNPDF3.0NLO	PYTHIA 8.230	A14	NLO
t t-channel	PowHEG-Box v2 [22–24, 38]	NNPDF3.0NLO	PYTHIA 8.230	A14	NLO
t s-channel	PowHEG-Box v2 [22–24, 39]	NNPDF3.0NLO	PYTHIA 8.230	A14	NLO
Multijet					
Dijets	PYTHIA 8.230	NNPDF2.3LO [44]	PYTHIA 8.230	A14	LO

4.1 Object Reconstruction

Charged particles reconstructed as tracks [72] in the inner detector form interaction vertices [73]. The primary vertex of the hard interaction is defined as the vertex with the highest sum of squared transverse momenta of associated tracks.

The anti- k_t algorithm implemented in FASTJET [15] is used to cluster large-radius ($R = 1.0$) jets from noise-suppressed topological energy depositions [74] calibrated to the local hadronic scale [75]. Jet cleaning criteria are used to identify jets arising from non-collision backgrounds or noise in the calorimeters [76] and events containing such jets are removed. Trimming jets reduces pile-up dependence and improves mass resolution [77]; subjets ($R=0.2$) with $p_T^i/p_T^{\text{jet}} < f_{\text{cut}}$ are removed, where p_T^i is the transverse momentum of the i^{th} subjet, and $f_{\text{cut}} = 0.05$. A weighted combination of the jet mass obtained from the calorimeter measurements with that from the charged component within the inner detector defines the jet mass m_J for a trimmed jet [78]. A series of simulation-based corrections and in situ techniques are applied to calibrate

p_T and m_J for jets within $|\eta| < 2$ [78].

The variable radius (VR) jet algorithm [79] forms track-jets from tracks compatible with the primary vertex [80]. They are associated with jets before trimming using ghost association [81, 82]. Simulated track-jets are labeled as b -, c - or light-flavor according to which hadrons with $p_T > 5$ GeV are found within $\Delta R = 0.3$ of the jet axis [83].

A multivariate discriminant (MV2) [83] is used to tag track-jets containing a b -hadron decay (b -tagged). The selection is tuned to produce an average efficiency of 77% for b -jets in simulated $t\bar{t}$ events, which corresponds to a light-flavor jet (u -, d -, s -quark, and gluon) and c -jet misidentification efficiency of 0.9% and 25%, respectively. Both in data and simulated events, jets with overlapping track-jets² are not considered for b -tagging as flavor-labeling is unreliable.

Muons are required to have $|\eta| < 2.4$, $p_T^\mu > 10$ GeV, and small impact parameters, as well as satisfy the ‘medium’ quality criterion [84]. Isolated muons additionally must satisfy loose track- and calorimeter-based isolation conditions.

4.2 Analysis Object Definitions

Reconstructed jets possessing properties compatible with an $H \rightarrow b\bar{b}$ decay are labeled *candidate jets*. The reconstructed jet containing the Higgs boson decay products, or H -jet, is not always the highest p_T jet in the event. Undetected neutrinos from semi-leptonic b -hadron decays further motivate considering the subleading jet. In around 50% and 47% of simulated ggF events, the H -jet is the leading and subleading p_T jet, respectively. Therefore, candidate jets are either of the two leading p_T jets with $|\eta| < 2$, $p_T > 250$ GeV, and $m_J > 60$ GeV. Furthermore, they must contain at least two track-jets.

A candidate jet is *double-tagged* if its two leading track-jets are b -tagged and *anti-tagged* if neither are b -tagged.

A ‘muon-in-jet’ correction is applied to candidate jets to account for the presence of semi-leptonic b -hadron decays. It utilizes the leading p_T muon found within $\Delta R < \min(0.4, 0.04 + 10/p_T^\mu)$ of a b -tagged track-jet. The scheme adds the muon four-momentum to the trimmed jet and removes the energy deposited by the muon in the calorimeter. After correcting 13% of leading and 33% of subleading H -jets in simulated ggF events, a 5% and 12% reduction in the m_J width, respectively, is observed. Henceforth, p_T and m_J refer to the corrected jet transverse momentum and mass, respectively, and p_T^u and m_J^u represent the uncorrected versions.

4.3 Experimental Systematic Uncertainties

The major experimental uncertainties originate from the jet mass resolution (JMR) modeling and jet mass-scale (JMS) calibration. Uncertainties on b -tagging correction factors and the jet energy scale play a minor role. The remaining uncertainties, including those arising from muon trigger, reconstruction, identification, and isolation rate modeling [84], are estimated to be negligible.

A ratio of calorimeter-based to track-based measurements in dijet data and simulation defines the uncertainties in the jet energy and mass scales [78]. Jet energy scale and mass uncertainties are divided into

² Track-jets “overlap” if the ΔR between them is less than the smaller of the two variable radii.

23 and 6 separate components, respectively. JMS uncertainties for $t\bar{t}$ events remain separated from those for V +jets and H events within the global likelihood discussed in Section 8. The dominant component in terms of reconstructed mass scale is further separated to act independently on all processes ($t\bar{t}$, V +jets, and H) and in all analysis p_T bins. Jet observables in the simulation are smeared to assess the impact of energy scale and mass resolution uncertainties. Consistent with previous studies for trimmed jets [85, 86], the energy resolution has an absolute 2% uncertainty, while the mass resolution has a relative 20% uncertainty. JMR uncertainties act independently on each process ($t\bar{t}$, V +jets, and H) and in each analysis p_T bin. The Z +jets JMR uncertainty is reduced using independent measurements described in Section 7.2.1.

The impact of uncertainties on b -tagging rates for b -, c -, and light-flavor jets are determined separately in various kinematic regions [83, 87, 88]. Each flavor category uncertainty is decomposed into independent components. A specific component for each jet flavor accounts for an extrapolation of the correction factor to jets with p_T beyond the calibration dataset kinematic reach. The thresholds are 250 GeV, 140 GeV, and 300 GeV for b -, c - and light-flavor track-jets, respectively.

5 Event categorization

Events are classified into three orthogonal regions, a signal region (SR), a $t\bar{t}$ control region ($CR_{t\bar{t}}$), or a validation region (VR) used to study the multijet and V +jets background models. In all instances, data are divided into kinematical regions depending on a jet p_T .

5.1 Signal and Validation Regions

A uniform requirement for both the VR and SR in all data taking years of at least one jet with $p_T^u > 450$ GeV and $m_J^u > 60$ GeV removes the kinematic regime biased by the trigger requirements. A second jet with $p_T^u > 200$ GeV is required to ensure a dijet topology. At least one of the two leading jets must satisfy the candidate jet criteria.

To categorize events, first, the leading jet is considered. If it is a double-tagged candidate jet, the event populates the leading-jet signal region (SRL). Failed events occupy the subleading-jet signal region (SRS) if the subleading jet is a double-tagged candidate jet. Approximately 40% of the H events surviving the kinematic cuts pass the b -tagging requirement.

The validation region always considers both leading jets. The leading-jet validation region (VRL) includes events where the leading jet is an anti-tagged candidate jet, and the subleading jet either has the same distinction or is not a candidate jet. An analogous definition defines the subleading-jet validation region (VRS).

The SRS has a sensitivity approximately 50% lower than that of the SRL. The principal reason being that jets containing b -hadron decays involving neutrinos exhibit a downward bias in their jet p_T measurement, which leads to a degradation of the mass resolution.

The analysis is performed with an inclusive signal region containing jets with $p_T > 250$ GeV, two fiducial signal regions and three differential signal regions. Lower p_T requirements on the candidate jet at 450 GeV and 1 TeV define two fiducial signal regions. Three differential signal regions are defined by requiring the candidate jet p_T to be between 250–450 GeV, 450–650 GeV, and 650–1000 GeV. Only the subleading-jet

Table 2: A summary of the $CR_{t\bar{t}}$ selection criteria.

Jet	N track-jets	N b -tags	Angular Selection
J_b	≥ 1	1	$0.04 + 10/p_T^\mu < \Delta R(\mu, J^b) < 1.5$
J_t	≥ 3	1	$\Delta\phi(J^b, J^t) > \frac{2\pi}{3}$

SR populates the lowest p_T region and only the leading-jet SR is used for highest p_T region, $p_T > 1$ TeV. The VRs follow the same definition.

Within each region, the discriminating variable is m_J . The combination of the $m_J^u > 60$ GeV selection and the muon-in-jet correction causes a reduced acceptance for m_J values near the selection threshold. Since the b -tagging efficiency diminishes with decreasing angular distance to another hadronic object [89], the low m_J region in the signal region is further sculpted. The prevalence of each effect determines the lowest m_J values studied. Therefore, the SR mass range examined in each region is 70 GeV or 75 GeV depending on the jet being the leading or the subleading and the p_T range considered, to 210 GeV. The VRs are studied using the same p_T bins and m_J range as the SRs.

5.2 $t\bar{t}$ Control Region

A dedicated $t\bar{t}$ control region, $CR_{t\bar{t}}$, using muon-trigger events, provides data with a high purity of top-quark pair events to determine the $t\bar{t}$ yield in conditions equivalent to those of the SRs.

The reconstructed final state is a top-quark system, one decaying leptonically and the other hadronically, in opposite detector hemispheres. An isolated muon, with $p_T^\mu > 52.5$ GeV, close to a jet J_b containing at least one track-jet defines the former, and a jet J_t with at least three track-jets defines the latter. Both jets are required to have $p_T > 250$ GeV and exactly one b -tagged track-jet. Considering multiple track-jets within J_b improves the identification efficiency of a b -quark reconstructed as a large- R jet.

To resemble the kinematics of top-quarks reconstructed in the SR, the $CR_{t\bar{t}}$ only contains events with $140 \text{ GeV} < m_{J_t} < 200 \text{ GeV}$, removing those where J_t does not contain all the top-quark decay products. Furthermore, to rectify differences in the $CR_{t\bar{t}}$ J_t and in the SRS candidate jet p_T spectrum below 450 GeV induced by different trigger requirements, $CR_{t\bar{t}}$ simulated $t\bar{t}$ events are reweighted and data events removed until the p_T spectra agree.

The same p_T boundaries used in the SR are also applied to $p_T^{J_t}$ to define the inclusive and differential $CR_{t\bar{t}}$. The selection criteria, summarized in Table 2, achieve over 95% purity in $t\bar{t}$ events.

6 Higgs boson modeling

The limited number of event selection criteria pertaining to properties of the recoil system or other activity in the event results in an inclusive analysis in terms of the Higgs boson production modes. Table 3 shows the relative contribution of the four main production modes as a function of Higgs boson candidate p_T , according to SM predictions. Only events within the Higgs boson window, defined by $105 < m_J < 140$ GeV, are considered. In both the SRL and SRS, ggF production contributes most for $p_T^{\text{jet}} > 450$ GeV. In SRS0,

Table 3: The fractional contribution of each production mode to a given analysis region around the Higgs boson peak, defined by $105 < m_J < 140$ GeV. The fraction is given with respect to the total yield in the analysis region in question.

Process	p_T Range [GeV]			
	250–450 GeV	450–650 GeV	650–1000 GeV	> 1000 GeV
SRL				
ggF	–	0.56	0.52	0.46
VBF	–	0.17	0.17	0.17
VH	–	0.14	0.15	0.20
$t\bar{t}H$	–	0.13	0.16	0.17
SRS				
ggF	0.28	0.46	0.43	–
VBF	0.07	0.19	0.21	–
VH	0.26	0.24	0.26	–
$t\bar{t}H$	0.39	0.11	0.10	–

$t\bar{t}H$ comprises around 40% of the Higgs boson events. A hadronically decaying top-quark can satisfy the jet trigger requirements without a high p_T^H value, thus resulting in a significant contribution of $t\bar{t}H$ events with relatively low Higgs boson p_T . Almost 90% of $t\bar{t}H$ events in the Higgs boson window arise from $H \rightarrow b\bar{b}$ decays. $H \rightarrow W^\pm W^\mp$ provides a majority of the remainder and climbs to almost 15% for larger m_J values.

The acceptance uncertainty on ggF-produced events is 20%. It includes variations of the factorization and renormalization scales, PDF, and parton shower model. Ref. [90] demonstrates that the NLO correction is nearly equivalent in the infinite top-mass approximation and full SM calculation; no additional systematic uncertainty is assigned. Acceptance uncertainties on the VBF, VH, and $t\bar{t}H$ processes are 0.5%, 5%, and 13%, respectively [32]. Systematic uncertainties on the EW corrections (expressed as $1 + \delta_{EW}$) are taken as δ_{EW}^2 following the recommendations in Ref. [5].

7 Background process modeling

Multijet production is the dominant background process. V +jets and $t\bar{t}$ resonance peaks flank the Higgs boson signal in low- and high-mass side-bands, respectively, but also leak into the Higgs boson signal window. Within $105 \text{ GeV} < m_J < 140 \text{ GeV}$, V +jets is 1.5% of the total background, $t\bar{t}$ accounts for 2%, and multijets provide the rest. The expected signal contribution equates to 0.2% of the background and 20-80% of the data statistical precision.

An accurate and precise determination of the background is paramount and is achieved starting with the determination of the V +jets and $t\bar{t}$ backgrounds.

7.1 Top-quark pair production

The $CR_{t\bar{t}}$ design ensures the same underlying physics process responsible for the SRs' events also populate the control region. The simulated J_t mass distribution in the CR and SR are similar in shape and peak near the top-quark mass because both regions probe a similar top-quark momentum range. Therefore, any adjustment of the simulated $t\bar{t}$ events made to improve the agreement with data in the $CR_{t\bar{t}}$ can be directly applied to the SR. This is achieved by including the $CR_{t\bar{t}}$ in the global likelihood described in Section 8. $CR_{t\bar{t}} 0$, $CR_{t\bar{t}} 1$, and $CR_{t\bar{t}} 2$ have a $t\bar{t}$ purity of 98%, 97%, and 95%, respectively. Single top-quark, W +jets, and multijet production provide the rest. With such high purity, the $t\bar{t}$ normalization is determined directly from data with 7–10% precision.

7.1.1 Systematic Uncertainties

Comparisons between nominal and alternative simulated samples provide modelling systematic uncertainty estimates for the parton shower model (Herwig 7 replaces PYTHIA 8) and the matrix element calculation (MADGRAPH5_aMC@NLO replaces POWHEG-Box v2). The comparisons show a 6–20% and 1–19% difference in yield in the various analysis regions, respectively. Within the nominal sample, variations of internal weights are used to estimate the systematic uncertainty associated with initial and final state radiation (1–7%), as well as the renormalization and factorization scales (negligible).

All experimental errors described in Section 4.3 are utilized. Uncertainties on b -tagging efficiency of b -jets and JMS have the largest impact on the $t\bar{t}$ normalization.

Figure 2 shows the J_t mass distribution for each analysis p_T bin after the global likelihood fit in the differential configuration. The simulation agrees well with the data.

7.2 V +jets production

With a decay structure and relative experimental resolution similar to that of the Higgs boson, the vector boson mass peaks offer a unique opportunity to validate experimental performance.

In the VR, W events outnumber Z events nearly three to one due to the larger cross section and comparable acceptance. In the SR, the Z events outnumber W events over three to one due to the sizeable $Z \rightarrow b\bar{b}$ branching fraction and flavor tagging requirements. Z events outnumber H events by over a factor of 20. Experimental effects challenging to discern in a statistically-limited H production measurement will be evident in the Z observation. A well-understood Z measurement is therefore a precursor to a robust H measurement.

7.2.1 Systematic Uncertainties

As the data directly determines the Z +jets normalization, only modelling systematic uncertainties on the acceptances are relevant. The W +jets cross section carries a 10% uncertainty [91]. The maximum of seven independent pairs of renormalization and factorization scale variations by factors of 0.5 and 2 corresponds to a 3–20% error on the expected acceptance. An alternate PDF set (MMHT2014nlo), α_s variations within the nominal PDF set, and changing the cluster fragmentation model to the Lund string model [92] did not lead to a significant difference in the acceptance estimate of the nominal model.

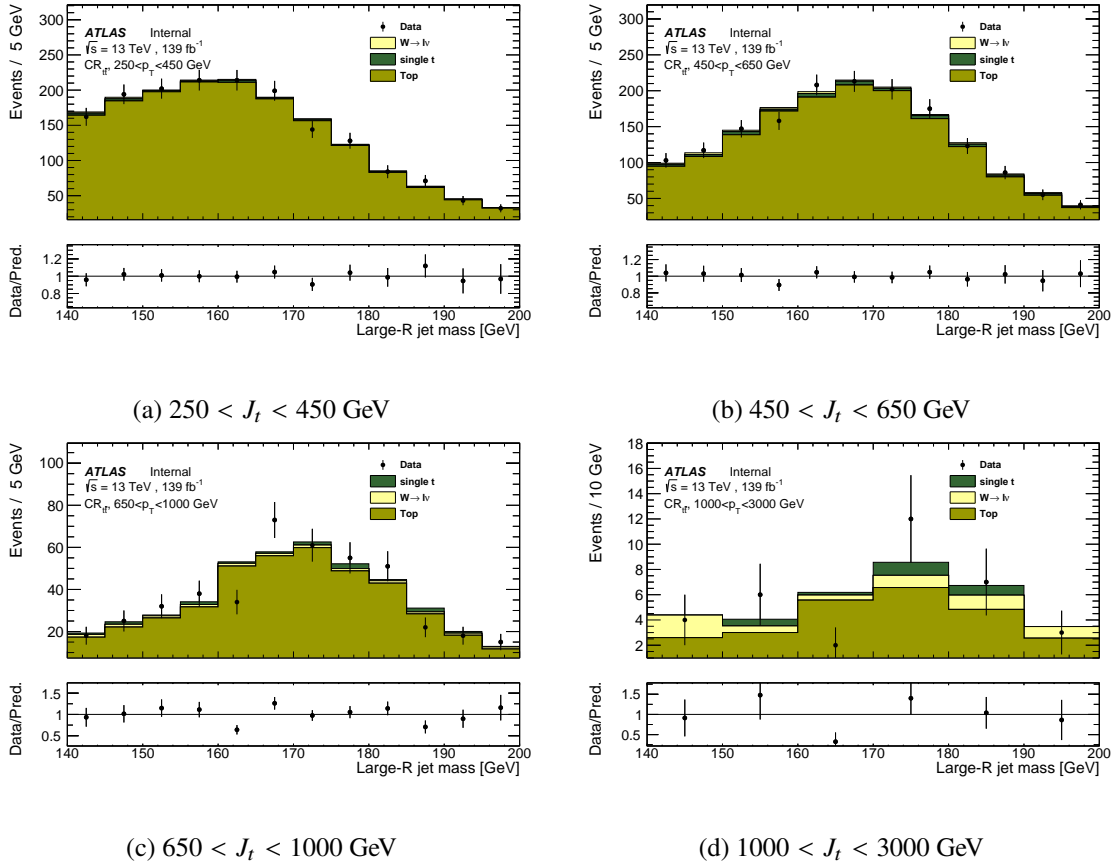


Figure 2: The post-fit $CR_{t\bar{t}} J_t$ mass distribution in the different p_T regions.

All experimental uncertainties described in Section 4.3 are applied. Uncertainties on JMR and JMS have the largest impact on the V +jets normalization. Using the full likelihood model described in Section 8 the leading large- R jet invariant mass distribution in the validation region is described to the level of agreement between simulation and data shown in Figure 3.

Jet Mass Resolution Uncertainty

The fitted Z normalization shows a significant correlation with the reconstructed m_J resolution uncertainty because the interaction of the Z + jets component in the mass spectrum and the multijet model flexibility opens a local minimum. Tests using subsets of the hybrid validation region, constructed to have a known amount of each process and discussed in the next section, highlight this feature. In some instances, the JMR parameter broadens the Z + jets peak. It corresponds to a Z + jets normalization increase and a multijet contribution decrease from the expected values.

To stabilize the fit response, the Z and W resonance jet mass widths are measured directly on two data samples and added as an additional constraint in the global likelihood. The two data samples are an alternate $t\bar{t}$ CR ($WCR_{t\bar{t}}$) and the VRL. The $WCR_{t\bar{t}}$ consists of selected semi-leptonic $t\bar{t}$ events having a resolved Wb pair from a hadronically decaying top-quark providing a high-purity reconstructed W peak

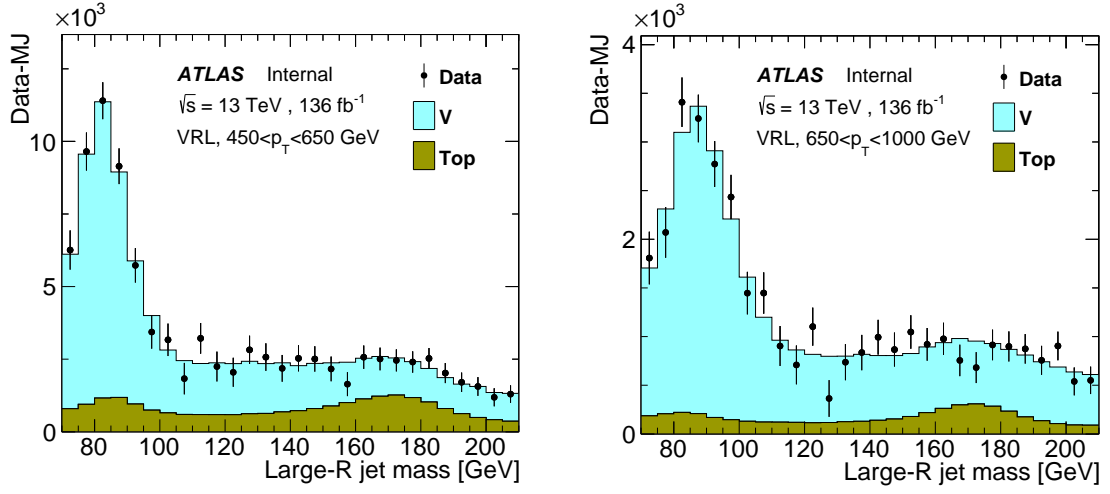


Figure 3: Post-fit leading large- R jet invariant mass distributions after the multijet background subtraction in the validation region for data (points with error bars) and the V +jets and $t\bar{t}$ components (histograms) for $450 < p_T < 650$ GeV (left) and $650 < p_T < 1000$ GeV (right).

with jet p_T from 200 GeV up to about 600 GeV. The VRL provides a clear W peak and covers the entire jet p_T range of this analysis but has considerably larger multijet contribution.

The measured jet mass width of the W and Z resonances shows a smooth evolution from low p_T in the $WCR_{l\bar{l}}$ to high p_T of the VRL (see Figure 4). These results inform an adjustment of the nominal jet mass resolution and reduce the JMR uncertainty to 14–22% of its original impact for Z + jets events, thus reducing the correlation between the Z + jets normalization and multijet functional form parameters.

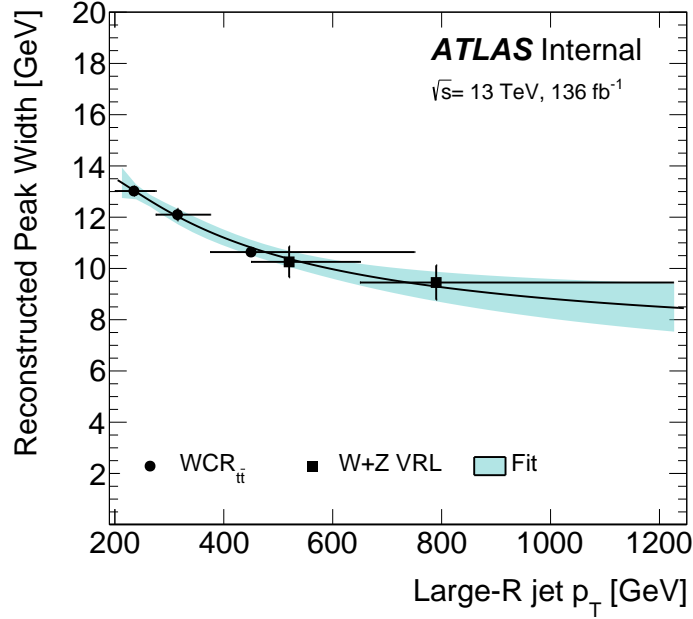


Figure 4: A summary of the Z and W resonance peak reconstructed width measurements as a function of the jet p_T using the resolved W in top-quark decays in the $WCR_{t\bar{t}}$ region and the W+Z in the validation region. The horizontal bars cover the jet p_T range used for the corresponding point and the points are centered at the average jet p_T in the same range. The continuous black curve is a fit to the measurements with resultant errors shown as a dark grey band.

7.3 Multijet production

An exponential of polynomial functions is used to model the multijet contribution

$$f_N(x|\vec{\theta}) = \theta_0 \exp\left(\sum_{i=1}^N \theta_i x^i\right), \quad (1)$$

where $x = (m_J - 150 \text{ GeV})/80 \text{ GeV}$ and θ_i are the parameters of the fit. Parameter values are independently determined in each region simultaneously with the signal extraction. The optimal number of parameters, N in Equation 1, depends on the mass shape and number of events analyzed. The VRS (VRL) contains 51 (58) times the amount of SRS (SRL) data. Therefore, ‘ensemble tests’ using modified VR subsets with roughly the same number of events as the corresponding SR, referred to as hybrid VR slices (VR_{hyb}), are used to determine N .

The hybrid VR is the best available proxy for the SR. It is defined by replacing the VR resonance peaks with the SM prediction from the SR and correcting the underlying multijet shape for SR acceptance effects. The following procedure for determining the resonance and multijet shape in the VR and SR data is used. The VR multijet estimate (MJ_{VR}) is created from the average of the multijet model parameter values obtained from global likelihood fits to ten orthogonal subsets of the VR. The VR $V+$ jets and $t\bar{t}$ estimates (V_{VR} and $t\bar{t}_{\text{VR}}$) are created from the average post-fit $V+$ jets and $t\bar{t}$ contributions from the same ten fits to the VR. The SR multijet estimate (MJ_{SR}) is obtained from a global likelihood fit to the SR. Each VR_{hyb}^i slice is:

$$VR_{\text{hyb}}^i = (VR^i - V_{\text{VR}} - t\bar{t}_{\text{VR}}) \times \left(\frac{MJ_{\text{SR}}}{MJ_{\text{VR}}}\right) + V_{\text{SR}} + t\bar{t}_{\text{SR}} + H_{\text{SR}},$$

where VR^i is the full distribution in a VR slice and V_{SR} , $t\bar{t}_{SR}$, and H_{SR} are the nominal MC predictions for V +jets, $t\bar{t}$, and H production, respectively. Figure 5 displays the multijet shape in the p_T -binned SRs and VRs along with data from the VR slices.

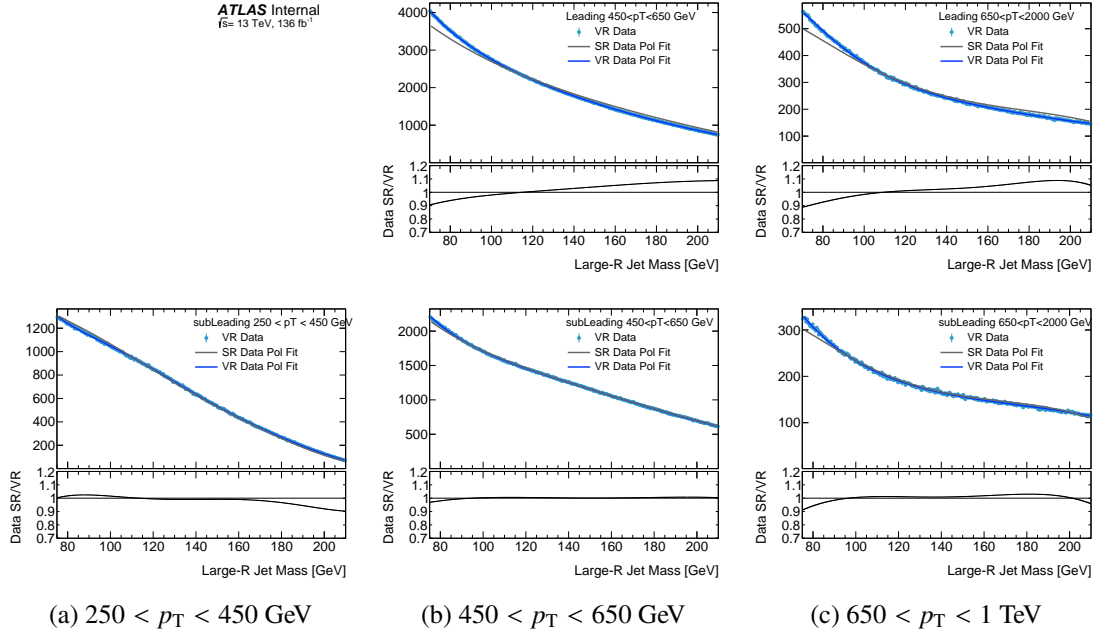


Figure 5: Comparison of the multijet shapes from the different p_T -binned analysis regions. The solid lines show the multijet function shape after a fit to the SR (gray) and VR (blue). The solid point are the data from VR slices. The $250 < p_T < 450$ GeV region is only populated in the subleading jet SR.

A procedure to choose the optimal N for each region utilizes three metrics evaluated with the VR_{hyb} collection. First, a log-likelihood ratio (LLR) test compares the result of an N -parameter fit (null hypothesis) to an $N + 1$ -parameter fit (alternative hypothesis) in each VR_{hyb} slice without any injected SM resonances. By Wilks' theorem, the likelihood ratio follows an asymptotic χ^2 distribution under the null hypothesis. The corresponding distribution of p -values is flat. The smallest N that yields a uniform distribution of p -values is selected.

The LLR test ensures a good description of the data over the full mass range, but resonance measurements are sensitive to local effects. Two rate tests sensitive to local effects rely on the fit result of a free normalization parameter and its associated error (generalized as $\mu^{VR} \pm \sigma_{stat}^{VR}$) on either the Z +jets process or the Higgs boson process. Both utilize VR_{hyb} slices with all SR resonances injected at the SM rates. $F_{2\sigma}$, the fraction of results where $|\mu^{VR} - 1|$ is beyond twice its error σ_{stat}^{VR} , estimates the probability that the multijet model allows substantial artificial excess or deficit.³ $\overline{\mu}/\sigma$ is the average value of $\mu^{VR}/\sigma_{stat}^{VR}$ and indicates a bias in determining the signal strength. N is incremented until $F_{2\sigma}$ is compatible with 0.05, and $\overline{\mu}/\sigma$ is compatible with 0.20 for both Z +jets and H production. The resultant N agrees when including systematic uncertainties and when not injecting the Z +jets and H processes into the VR_{hyb} slices. Five parameters are used in both inclusive regions while a mix of four and five parameters are used in the analysis p_T bins.

³ A 2σ threshold ensures some results from the full set of VR slices cross the boundary.

$\overline{\mu/\sigma}$ for the N chosen in each region indicates a bias in the background model. It defines the spurious signal systematic uncertainty and ranges from 0.01–0.33 for H and 0.15–0.65 for Z + jets production. In both cases, it has an insignificant impact on the sensitivity.

An alternative function, the Laurent series, provides a similar level of agreement with the multijet background in the VR_{hyb} collection. The differences between the two models are much smaller than the data statistical uncertainty and the expected Higgs boson yield. Therefore, the model choice does not motivate an additional systematic uncertainty.

8 Statistical analysis

Signal yields are extracted by minimizing the negative logarithm of a likelihood function $\mathcal{L}(\mu, \vec{\theta})$ with the RooStats framework [93]. The likelihood function is defined as the product of Poisson probability terms, one for each of the 5 GeV bins of the m_J distributions [94, 95]. The likelihood function is defined as the product of Poisson probability terms, one for each bin of the m_J distribution. Bin widths are set to 5 GeV, necessitating technical advancements to fit an analytic function to a wide-binned dataset [94, 95]. Systematic uncertainties enter the likelihood as nuisance parameters, $\vec{\theta}$, constrained with Gaussian or log-normal probability density function (PDF) priors. The JMR constraints obtained from the $WCR_{t\bar{t}}$ and VRL regions are included as Gaussian PDF priors. Unconstrained, or *free*, parameters control the normalization of the MC templates within each category and jet p_T range (SRL, SRS, and $CR_{t\bar{t}}$ when applicable, together) or within a given fiducial volume. For the multijet model, the function normalization and its polynomial coefficients are free parameters and independent for each region. Upper limits on the Higgs boson production cross section are derived using the CLs method [96, 97].

Signal yields are expressed as signal strengths, μ , obtained by normalizing the fitted number of signal events to the corresponding SM predictions. The cross sections are derived from the fitted signal yields divided by the integrated luminosity corrected by the product of the estimated selection efficiency and fiducial acceptance.

Table 4 summarizes the systematic uncertainties considered in the likelihood fit. In addition, uncertainties due to the limited number of events in the simulated samples used for the background predictions are parametrised using the Beeston–Barlow technique [98]. Systematic variations yielding large statistical fluctuations are smoothed using custom algorithms which also remove variations resulting in effects below 2% within each region.

Table 4: A summary of the systematic uncertainties included within the profile likelihood. For a given uncertainty, the second column lists each process which has independent nuisance parameters within the likelihood. The third column describes how the systematic uncertainty is correlated across regions: “all” indicates a fully correlated parameter, “ p_T bins” indicates a decorrelation between the analysis p_T bins, and “LS” means it is decorrelated between the SRL and SRS. For the inclusive analysis, “bins” does not apply, and should be understood to mean the same as “all”. The fourth column describes the change induced by the parameter. “S” means the m_J shape will change while “N” denotes parameters which change the normalization and can result in a migration of events between regions. (*) Two minor components separately apply to $t\bar{t}$ and V +jets events.

Description	Processes	Category	Effect
Experimental Systematics			
JMR	$t\bar{t}, V+\text{jets}, H$	p_T bins \times LS	S
JMS (dominant)	$t\bar{t}, V+\text{jets}, H$	p_T bins	N+S
JMS (rest)	$t\bar{t}, V+\text{jets}+H$	all	N+S
Jet energy scale	all ^(*)	all	N+S
Jet energy resolution	all	all	S
b -tag efficiency b -jets	all	all	N+S
b -tag efficiency c -jets	all	all	N+S
b -tag efficiency l -jets	all	all	N+S
Modeling Systematics			
Cross-section and acceptance	$W+\text{jets}$	all	N
Renormalization and factorization scale	$V+\text{jets}$	all	N+S
Parton shower model	$t\bar{t}$	all	N+S
Matrix element calculation	$t\bar{t}$	all	N+S
Initial-/Final-state radiation	$t\bar{t}$	all	N+S
Acceptance	H	all	N
NLO EW corrections	$\text{VBF}+VH+t\bar{t}H$	all	N
	$V+\text{jets}$	all	N
Spurious signal	H	p_T bins \times LS	N
	$Z+\text{jets}$	p_T bins \times LS	N

9 Results

The analysis regions designed to probe Higgs boson production with considerable transverse momentum are summarized in Table 5. They provide one all-encompassing region to determine the H signal strength, two regions for fiducial cross-section measurements, and three bins for a differential measurement.

All H events are considered for the signal strength extraction. For the fiducial and differential measurements, signal events within the fiducial volume defined by requirements on the generator ‘truth’ record detailed below, are counted. Within the global likelihood, the yield of signal events outside the targeted category are constrained to their SM prediction within the theoretical and experimental uncertainties.

The fiducial measurements extract the yield of events with Higgs bosons having $p_T^H > 450$ GeV and $p_T^H > 1$ TeV in the corresponding analysis regions, respectively. This configuration allows a straightforward comparison to theoretical calculations, such as those reported in Ref. [32].

Table 5: A summary of the names and definitions of the analysis regions used for the measurements. The lowest p_T bin is not populated in the leading-jet signal region. Following the definitions in Section 5.1, each SR has an associated VR in the same kinematic region. (*) Jets are ordered before the muon-in-jet correction is applied.

Considered Jet			Inclusive	Fiducial	Differential			
Type	N b -tags	Order*	p_{T} Range [GeV]					
			>250/450	>450	>1000	250–450	450–650	650–1000
Signal Regions								
Candidate	2	Lead	SRL	SRL	SRL	–	SRL1	SRL2
	2	Sublead	SRS	SRS	–	SRS0	SRS1	SRS2
$t\bar{t}$ Control Regions								
J^t	1	–	$CR_{t\bar{t}}$	$CR_{t\bar{t}}$	$CR_{t\bar{t}}$	$CR_{t\bar{t}} 0$	$CR_{t\bar{t}} 1$	$CR_{t\bar{t}} 2$

The differential measurement uses the analysis p_T regions to count H events separately for three p_T^H categories, following the regions defined in the stage-1.2 STXS scheme. This configuration affords enhanced sensitivity to BSM physics effects. The analysis jet p_T bins align well with the p_T^H -defined categories to maintain a low correlation between measurements. A few measurements can be motivated by the minimal definition of the recoil system. For example, dimension-6 EFT operators in the SILH basis [99], such as c_g (modifies the interactions between the Higgs boson and gluons) and c_{tg} (modifies the interactions between gluons and the top quark), motivate measuring $t\bar{t}H + \text{ggF}$ production. However, the enhancements corresponding to the c_g (c_{tg}) coefficients are 20–40 (2–4) times larger for ggF than $t\bar{t}H$, implying little sensitivity to $t\bar{t}H$. The non-negligible VBF and VH production modes can also complement more targeted results [100–102]. Therefore, the measurements presented in this paper count all production modes to minimize the dependence of theoretical assumptions. Using the same category definitions, differential cross-section measurements of $V + \text{jets}$ production in the VRL and $Z + \text{jets}$ production in the SR validate the method.

9.1 Inclusive region

The inclusive region yields a Higgs boson signal strength for the combination of SRL, SRS and $CR_{t\bar{t}}$ of $\mu_H = 1.1 \pm 3.6$. The fit χ^2 probability values are 0.19 and 0.77 for the SRL and SRS, respectively. Results are summarized in Table 6 and the yields in Table 7. The Higgs boson signal strength uncertainty is statistically dominated. The leading sources of systematic uncertainties are jet mass resolution and mass scale.

Table 6: Expected and observed values of the signal strengths for the H , Z and $t\bar{t}$ components in the inclusive fit. The values of $\mu_{t\bar{t}}$ obtained are in agreement with unfolded measurements of $t\bar{t}$ events in a similar kinematic phase-space [103].

Result	μ_H	μ_Z	$\mu_{t\bar{t}}$
Expected	1.0 ± 3.0	1.00 ± 0.17	1.00 ± 0.07
Observed	1.1 ± 3.6	1.25 ± 0.22	0.81 ± 0.06

Table 7: Event yields and associated uncertainties after the global likelihood fit in the inclusive region.

Process	SRL	SRS	$CR_{t\bar{t}}$
Multijet	591 400 \pm 4200	530 000 \pm 3500	–
Z	15 900 \pm 2700	11 800 \pm 2000	–
W	3070 \pm 700	2520 \pm 500	–
$t\bar{t}$	15 700 \pm 1900	15 300 \pm 2000	3663 \pm 65
$W(\ell\nu)$	–	–	53 \pm 1
single- t	–	–	74.1 \pm 1.5
H	500 \pm 1800	400 \pm 1400	–
Data	626 532	560 083	3777

9.2 Fiducial $p_T^H > 450$ GeV and $p_T^H > 1$ TeV regions

The two fiducial regions determine the Higgs boson yield and cross section in the phase space defined by the Higgs boson pseudo-rapidity range $|\eta_H| < 2.0$ and transverse momentum $p_T^H > 450$ GeV and $p_T^H > 1$ TeV. Compared to the inclusive measurement discussed above, the fiducial region for $p_T^H > 450$ GeV does not include the SRS region below 450 GeV. The $p_T^H > 1$ TeV region probes a new domain of highly boosted Z and Higgs boson reconstruction. Since the expected sensitivity in the SRS above 1 TeV is marginal as the muon-in-jet correction and b -tagging turn-on effects are more significant compared to the SRL, the measurement above 1 TeV is based only on the SRL and $CR_{t\bar{t}}$ regions. The acceptance times efficiency values for the different SM Higgs boson production processes are given in Table 8.

Table 8: Signal acceptance times efficiency for the signal regions in the fiducial measurements.

Process	$p_T^H > 450$ GeV	$p_T^H > 1$ TeV
All	0.25	0.18
ggF	0.26	0.22
VH	0.27	0.19
VBF	0.22	0.15
$t\bar{t}H$	0.20	0.16

Table 9: Expected and observed values of the signal strengths for the H , Z , and $t\bar{t}$ components in the fiducial fits. The value for μ_H refers to the fiducial volume $|\eta_H| < 2.0$, $p_T^H > 450$ GeV and $p_T^H > 1$ TeV, while those for μ_Z and $\mu_{t\bar{t}}$ pertain to regions of jet p_T above the 450 GeV and 1 TeV. The values of $\mu_{t\bar{t}}$ obtained are in agreement with unfolded measurements of $t\bar{t}$ events in a similar kinematic phase-space [103].

Region	μ_H		μ_Z		$\mu_{t\bar{t}}$	
	Expected	Observed	Expected	Observed	Expected	Observed
$p_T^H > 450$ GeV	1.0 ± 3.3	0.7 ± 3.3	1.00 ± 0.18	1.27 ± 0.22	1.00 ± 0.07	0.81 ± 0.06
$p_T^H > 1$ TeV	1.0 ± 29.0	26 ± 31	1.0 ± 1.6	2.4 ± 1.7	1.0 ± 0.3	0.51 ± 0.19

Two Higgs boson mass templates are used in the fiducial fits. The first describes the mass distribution of events with signal jet and Higgs boson p_T above the cut of choice; the second those with signal jet above the p_T cut but Higgs boson p_T below it. The first component accounts for more than 80% (70%) of the Higgs boson signal selected by the 450 GeV (1 TeV) jet p_T cut and its yield is left free in the fit, while the second is fixed to its SM value.

This procedure is first tested with $W \rightarrow qq'$ and $Z \rightarrow q\bar{q}$ in the VR and $Z \rightarrow b\bar{b}$ in the SR. For these tests, the V and Z mass templates are structured similarly to those of the Higgs boson described above and the Higgs boson yields are kept fixed to their SM expectations in the fit. In the VR, the fitted signal strengths for $W \rightarrow qq'$ and $Z \rightarrow q\bar{q}$ with $p_T^V > 450$ GeV and 1 TeV are $\mu_V = 1.01 \pm 0.09$ and 1.56 ± 0.50 , respectively. In the SR, the μ_Z values for $Z \rightarrow b\bar{b}$ with $p_T^Z > 450$ GeV and 1 TeV are 1.35 ± 0.23 and 2.6 ± 1.6 , respectively. These results are in agreement with the SM.

The Higgs boson fit result for $p_T^H > 450$ GeV provides a signal strength of $\mu_H = 0.7 \pm 3.3$ and for $p_T^H > 1$ TeV gives $\mu_H = 26^{+33}_{-30}$. These yields correspond to Higgs boson production cross section values in the fiducial region of

$$\begin{aligned}\sigma_H(p_T^H > 450 \text{ GeV}) &= 13 \pm 57 \text{ (stat.)} \pm 22 \text{ (syst.)} \pm 3 \text{ (theory) fb} \\ \sigma_H(p_T^H > 1 \text{ TeV}) &= 3.4 \pm 3.6 \text{ (stat.)} \pm 1.7 \text{ (syst.)} \pm 0.8 \text{ (theory) fb},\end{aligned}$$

and 95% confidence Level (CL) upper limits of

$$\begin{aligned}\sigma_H(p_T^H > 450 \text{ GeV}) &< 144 \text{ fb} \\ \sigma_H(p_T^H > 1 \text{ TeV}) &< 10.3 \text{ fb}.\end{aligned}$$

The post-fit SRL and SRS jet mass distributions are shown in Figure 6. Results are summarised in Table 9. The uncertainties are statistically dominated. The contributions of the main categories of systematic uncertainties are given in Table 10. The jet systematics give the largest contribution, driven by the JMS effects at lower p_T and by JMR above 1 TeV where the constraints are looser due to the extrapolation uncertainties (see Figure 4). Similarly, the flavour tagging uncertainties increase above 1 TeV due to the extrapolation from the p_T range of the calibration regions.

Table 10: Contributions to the systematic uncertainties for the fiducial signal strength measurements. The total uncertainty is also given for comparison.

Uncertainty Contribution	$p_T^H > 450$ GeV	$p_T^H > 1$ TeV
Statistical+Systematic	3.3	31.4
Jet Systematics	1.20	7.02
Modelling and Theory Sysys.	0.95	0.99
Flavor Tagging Sysys.	0.48	3.04

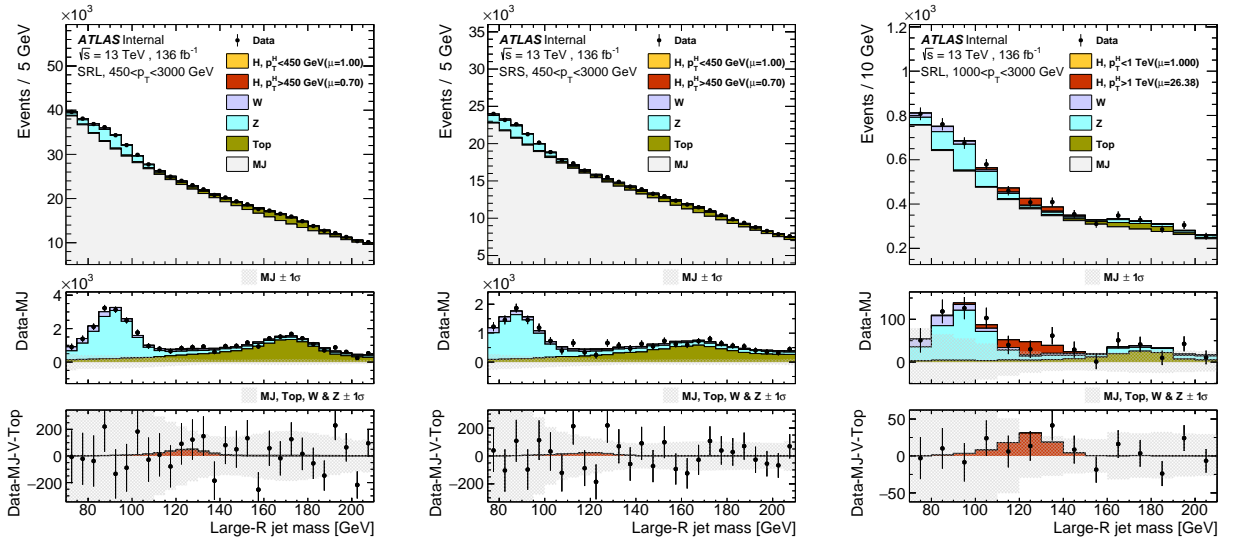


Figure 6: Post-fit signal jet mass distributions for the fiducial regions with $p_T^H > 450$ GeV in the SRL (left), SRS (center) and with $p_T^H > 1$ TeV in the SRL (right) with the various components. The lower panels show the distributions after subtraction of the multijet distribution and, additionally, the V + jets and $t\bar{t}$ fitted contributions. The shaded areas indicate the 68% C.L. for the multijet background from the fitted parameters and normalisations of the exponential polynomials.

9.3 Differential regions

The differential regions aim to measure the differential spectrum of the Higgs boson transverse momentum, where possible deviations from the SM predictions could manifest with an amplitude increasing with p_T^H . Extending the procedure adopted for the fiducial measurements, several Higgs boson mass templates corresponding to same jet p_T but different p_T^H ranges are used in the fits. Figure 7 presents the signal yield in each reconstructed-event category for each fiducial volume and the corresponding fraction of signal events.

The procedure is tested with $W \rightarrow qq'$ and $Z \rightarrow q\bar{q}$ in the VR and $Z \rightarrow b\bar{b}$ in the SR. The VR offers a sample with larger statistics although lower signal-to-background ratio. For the differential V + jets analysis, the VRL is divided in five slices, the fit performed independently on each slice and the results combined.

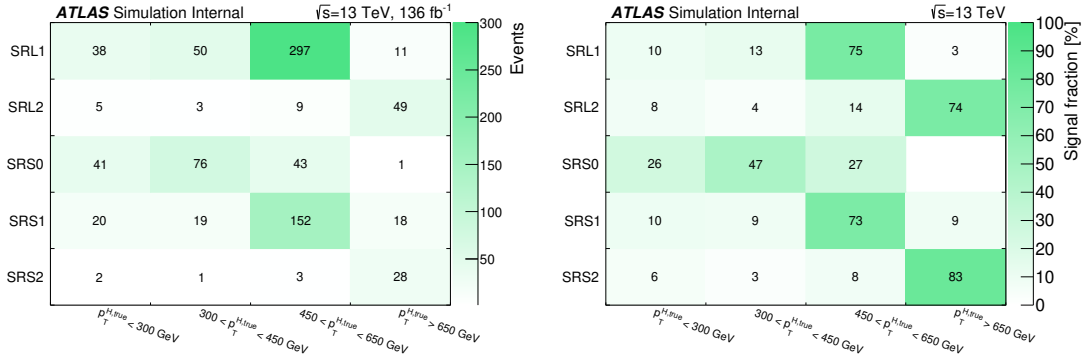


Figure 7: For each of the differential regions, signal event yield for all Higgs boson events (left) and the fraction of signal (in percent) (right) in each reconstructed region vs. the differential signal region.

In the SR the differential Z fit is performed to the SRL, SRS, and $CR_{l\bar{l}}$ regions. Results of the two fits are shown in Figure 8 where they are compared to the predictions for the EW NLO and QCD NNLO k-factors as a function of p_T^V . Both results agree with SM expectations.

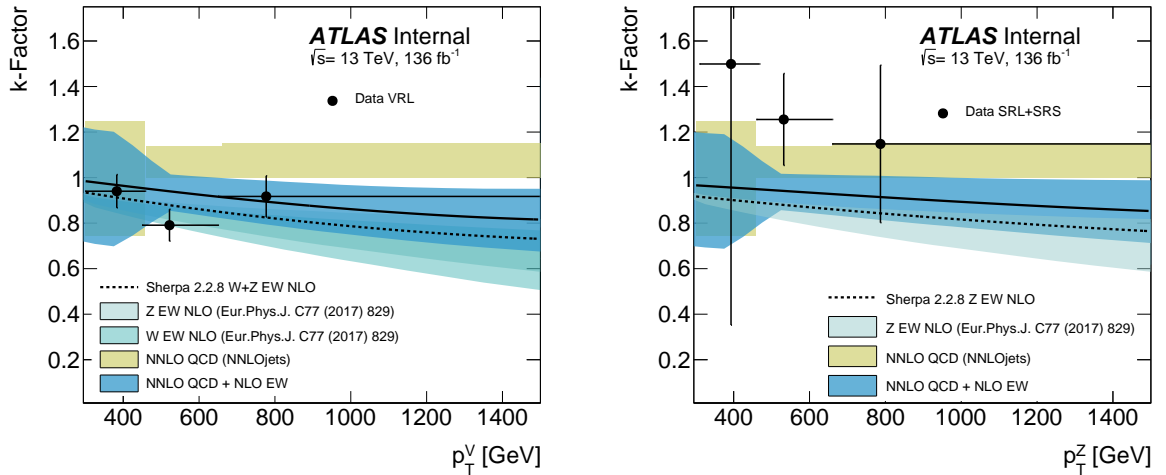


Figure 8: Comparison of V+jets k-factors with the differential fit results in the VRL (left) and SR (right). Differential fit results are rescaled by the ratio of the cross sections predicted by Sherpa with and without the NLO EW correction weights and are compared to calculations at NLO EW, NNLO QCD and their product.

The eight differential SR and CR regions defined in Table 5 are simultaneously fitted exploiting the corresponding systematic configurations shown in Table 4. Results are summarised in Table 11. The post-fit jet mass distribution from the most sensitive category in each jet p_T bin is shown in Figure 9.

The acceptance times efficiency values for the different Higgs boson production processes are given in Table 12. The resulting Higgs boson production cross section for $p_T^H > 650$ GeV is 13 ± 16 (stat.) ± 7 (syst.) ± 3 (theory) fb. The differential results correspond to the following 95% CL upper limits on the

Table 11: Expected and observed values of the signal strengths for the H , Z , and $t\bar{t}$ components in the differential fits. The value for μ_H refers to a fiducial p_T^H volume, while those for μ_Z and $\mu_{t\bar{t}}$ pertain to the corresponding jet p_T regions. The values of $\mu_{t\bar{t}}$ obtained are in agreement with unfolded measurements of $t\bar{t}$ events in a similar kinematic phase-space [103].

Region	μ_H		μ_Z		$\mu_{t\bar{t}}$	
	Expected	Observed	Expected	Observed	Expected	Observed
$300 < p_T^H < 450$ GeV	1 ± 18	-7 ± 17	1.00 ± 1.11	1.87 ± 1.20	1.00 ± 0.07	0.87 ± 0.06
$450 < p_T^H < 650$ GeV	1.0 ± 3.3	-2.9 ± 4.7	1.00 ± 0.17	1.37 ± 0.23	1.00 ± 0.07	0.76 ± 0.06
$p_T^H > 650$ GeV	1.0 ± 6.3	4.8 ± 6.4	1.00 ± 0.33	1.45 ± 0.45	1.00 ± 0.09	0.74 ± 0.07

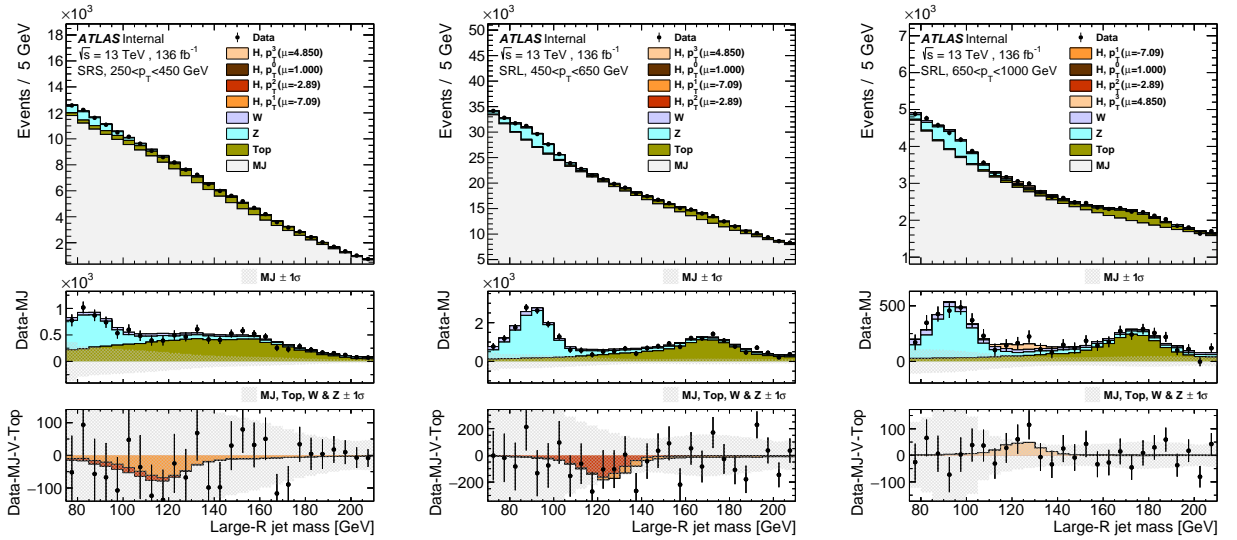


Figure 9: Post-fit signal jet mass distributions for the differential regions from SRS0 (left), SRL1 (center) and SRL2 (right) with the various components. The lower panels show the distributions after subtraction of the multijet distribution and, additionally, the V +jets and $t\bar{t}$ fitted contributions. The shaded areas indicate the 68% CL for the multijet background from the fitted parameters and normalisations of the exponential polynomials.

Higgs boson differential production cross sections:

$$\sigma_H(300 < p_T^H < 450 \text{ GeV}) < 2.8 \text{ pb};$$

$$\sigma_H(450 < p_T^H < 650 \text{ GeV}) < 91 \text{ fb};$$

$$\sigma_H(p_T^H > 650 \text{ GeV}) < 40.5 \text{ fb}.$$

The uncertainties are statistically dominated. The contributions of the main categories of systematic uncertainties are summarised in Table 13. The $t\bar{t}$ modelling systematic uncertainties are more relevant in the first jet p_T bin and decrease above 450 GeV, where the top-quark decay products become more collimated thus reducing the contamination around the Higgs boson mass peak.

Table 12: Signal acceptance times efficiency for the signal regions in the differential measurements.

Process	$300 < p_T^H < 450 \text{ GeV}$	$450 < p_T^H < 650 \text{ GeV}$	$p_T^H > 650 \text{ GeV}$
All	1.4×10^{-2}	0.25	0.33
ggF	0.7×10^{-2}	0.26	0.37
VH	1.8×10^{-2}	0.28	0.31
VBF	0.2×10^{-2}	0.14	0.18
$t\bar{t}H$	4.9×10^{-2}	0.20	0.25

Table 13: Contributions to the systematic uncertainties for the differential signal strength measurements. The total uncertainty is also given for comparison.

Uncertainty Contribution	$300 < p_T^H < 450 \text{ GeV}$	$450 < p_T^H < 650 \text{ GeV}$	$p_T^H > 650 \text{ GeV}$
Statistical+Systematic	17	4.7	6.4
Jet Systematics	5.4	2.6	2.3
Modelling and Theory Sys.	3.8	< 0.1	0.14
Flavour Tagging Sys.	< 0.1	< 0.1	< 0.1

10 Conclusions

Studies of the Higgs boson produced at high p_T and decaying into $b\bar{b}$ pair are performed. The results are based on the Run 2 dataset of pp collision data collected at $\sqrt{s} = 13 \text{ TeV}$ by the ATLAS detector at the LHC, corresponding to an integrated luminosity of 136 fb^{-1} . The Higgs boson is reconstructed from a single large- R jet and identified with b -tagging techniques. Two fiducial measurements and a differential measurement are performed in regions of increasing p_T^H . Within the same kinematic regimes, measurements of the $Z \rightarrow b\bar{b}$ process agree with the Standard Model predictions, validating the methods.

The Higgs boson production cross section for $p_T^H > 450 \text{ GeV}$ is measured to be $13 \pm 57(\text{stat.}) \pm 22(\text{syst.}) \pm 3(\text{theory}) \text{ fb}$ and for $p_T^H > 1 \text{ TeV}$ it is measured to be $3.4 \pm 3.6(\text{stat.}) \pm 1.7(\text{syst.}) \pm 0.8(\text{theory}) \text{ fb}$. Higgs boson cross-section production limits at 95% CL obtained in four differential volumes, following the simplified cross-section framework, are: $\sigma_H(300 < p_T^H < 450 \text{ GeV}) < 2.8 \text{ pb}$, $\sigma_H(450 < p_T^H < 650 \text{ GeV}) < 91 \text{ fb}$, $\sigma_H(p_T^H > 650 \text{ GeV}) < 40.5 \text{ fb}$, and $\sigma_H(p_T^H > 1 \text{ TeV}) < 10.3 \text{ fb}$. All of the Higgs boson results agree with the Standard Model predictions.

Appendix

Not reviewed, for internal circulation only

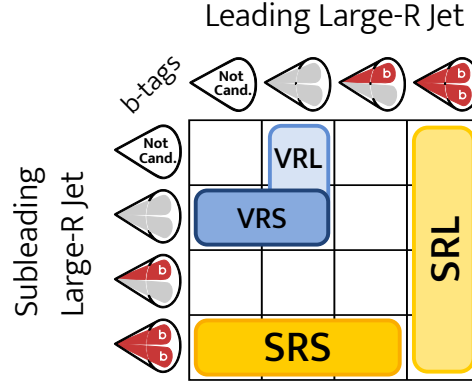


Figure 10: Diagram showing the event categorization criteria. The columns (rows) are divided into 4 categories: when the leading (subleading) jet is not a candidate jet (see Section 4.2), when neither of the first two p_T -ordered track-jet is b -tagged, when one of the track-jets is b -tagged and when both track-jets are b -tagged.

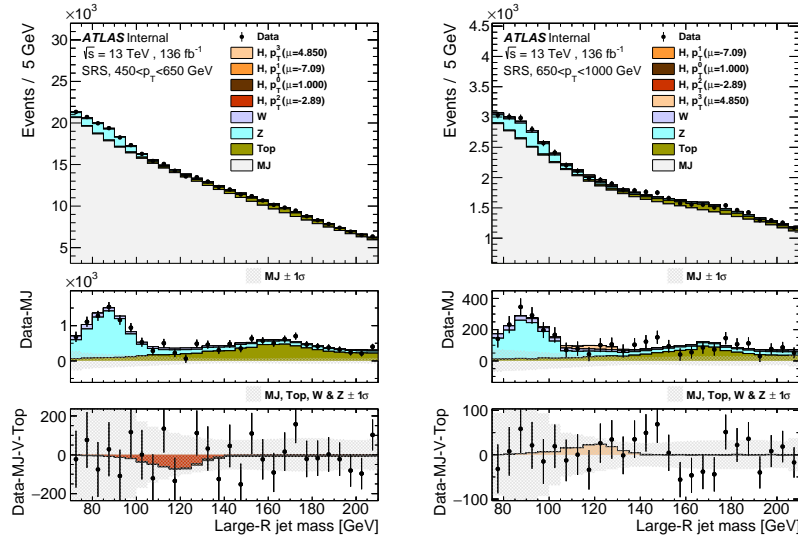


Figure 11: Post-fit signal jet mass distributions for the differential regions from SRS1 (left), SRS2 (right) with the various components. The lower panels show the distributions after subtraction of the multijet distribution and, additionally, the V + jets and $t\bar{t}$ fitted contributions. The shaded areas indicate the 68% CL for the multijet background from the fitted parameters and normalisations of the exponential polynomials.

Table 14: Event yields and associated uncertainties after the global likelihood fit of the differential regions.

Process	SRL1	SRL2	SRS0	SRS1	SRS2	$CR_{t\bar{t}}^0$	$CR_{t\bar{t}}^1$	$CR_{t\bar{t}}^2$
QCD	510200 ± 3600	72500 ± 1100	157600 ± 2900	341100 ± 2100	48160 ± 710	—	—	—
$Z(jj)$	13100 ± 2200	2570 ± 770	3900 ± 2400	8000 ± 1300	1610 ± 520	—	—	—
$W(jj)$	2280 ± 490	630 ± 150	770 ± 140	1380 ± 260	365 ± 84	—	—	—
$t\bar{t}$	12600 ± 1200	2290 ± 290	7800 ± 1000	6870 ± 740	1060 ± 160	1656 ± 42	1568 ± 41	415 ± 21
$W(\ell\nu)$	—	—	—	—	—	11.9 ± 0	22.3 ± 0	13.6 ± 0
single- t	—	—	—	—	—	19.9 ± 0	39.5 ± 0	12.2 ± 0
H pT0	38.1 ± 0	5 ± 0	41.1 ± 0	19.7 ± 0	2 ± 0	—	—	—
H pT1	-360 ± 870	-19 ± 45	-500 ± 1300	-130 ± 320	-6 ± 16	—	—	—
H pT2	-900 ± 1400	-27 ± 44	-120 ± 200	-440 ± 710	-8 ± 13	—	—	—
H pT3	54 ± 71	240 ± 310	3.3 ± 4.4	90 ± 110	140 ± 180	—	—	—
Data	537038	78177	169418	356910	51324	1687	1628	442

References

- [1] ATLAS Collaboration, *Observation of a new particle in the search for the Standard Model Higgs boson with the ATLAS detector at the LHC*, *Phys. Lett. B* **716** (2012) 1, arXiv: [1207.7214 \[hep-ex\]](#) (cit. on p. 2).
- [2] CMS Collaboration, *Observation of a new boson at a mass of 125 GeV with the CMS experiment at the LHC*, *Phys. Lett. B* **716** (2012) 30, arXiv: [1207.7235 \[hep-ex\]](#) (cit. on p. 2).
- [3] ATLAS Collaboration, *Combined measurements of Higgs boson production and decay using up to 80fb^{-1} of proton–proton collision data at $\sqrt{s} = 13\text{ TeV}$ collected with the ATLAS experiment*, *Phys. Rev. D* **101** (2020) 012002, arXiv: [1909.02845 \[hep-ex\]](#) (cit. on p. 2).
- [4] CMS Collaboration, *Combined measurements of Higgs boson couplings in proton–proton collisions at $\sqrt{s} = 13\text{ TeV}$* , *Eur. Phys. J. C* **79** (2019) 421, arXiv: [1809.10733 \[hep-ex\]](#) (cit. on p. 2).
- [5] D. de Florian et al., *Handbook of LHC Higgs Cross Sections: 4. Deciphering the Nature of the Higgs Sector*, (2016), arXiv: [1610.07922 \[hep-ph\]](#) (cit. on pp. 2, 10).
- [6] J. R. Andersen et al., “Les Houches 2015: Physics at TeV Colliders Standard Model Working Group Report,” *9th Les Houches Workshop on Physics at TeV Colliders (PhysTeV 2015) Les Houches, France, June 1-19, 2015*, 2016, arXiv: [1605.04692 \[hep-ph\]](#), URL: <http://lss.fnal.gov/archive/2016/conf/fermilab-conf-16-175-ppd-t.pdf> (cit. on p. 2).
- [7] N. Berger et al., *Simplified Template Cross Sections - Stage 1.1*, (2019), arXiv: [1906.02754 \[hep-ph\]](#) (cit. on p. 2).
- [8] C. Grojean, E. Salvioni, M. Schlaffer, and A. Weiler, *Very boosted Higgs in gluon fusion*, *JHEP* **05** (2014) 022, arXiv: [1312.3317 \[hep-ph\]](#) (cit. on p. 3).
- [9] A. Biekötter, A. Knochel, M. Krämer, D. Liu, and F. Riva, *Vices and virtues of Higgs effective field theories at large energy*, *Phys. Rev. D* **91** (2015) 055029, arXiv: [1406.7320 \[hep-ph\]](#) (cit. on p. 3).
- [10] K. Mimasu, V. Sanz, and C. Williams, *Higher Order QCD predictions for Associated Higgs production with anomalous couplings to gauge bosons*, *JHEP* **08** (2016) 039, arXiv: [1512.02572 \[hep-ph\]](#) (cit. on p. 3).
- [11] M. Grazzini, A. Ilnicka, M. Spira, and M. Wiesemann, *Modeling BSM effects on the Higgs transverse-momentum spectrum in an EFT approach*, *JHEP* **03** (2017) 115, arXiv: [1612.00283 \[hep-ph\]](#) (cit. on p. 3).
- [12] A. Banfi, A. Bond, A. Martin, and V. Sanz, *Digging for Top Squarks from Higgs data: from signal strengths to differential distributions*, *JHEP* **11** (2018) 171, arXiv: [1806.05598 \[hep-ph\]](#) (cit. on p. 3).
- [13] ATLAS Collaboration, *The ATLAS Experiment at the CERN Large Hadron Collider*, *JINST* **3** (2008) S08003 (cit. on pp. 3, 4).

- [14] CMS Collaboration, *Inclusive search for highly boosted Higgs bosons decaying to bottom quark-antiquark pairs in proton–proton collisions at $\sqrt{s} = 13$ TeV*, *JHEP* **12** (2020) 085, arXiv: [2006.13251 \[hep-ex\]](#) (cit. on p. 3).
- [15] M. Cacciari, G. P. Salam, and G. Soyez, *FastJet user manual*, *Eur. Phys. J. C* **72** (2012) 1896, arXiv: [1111.6097 \[hep-ph\]](#) (cit. on pp. 4, 6).
- [16] ATLAS Collaboration, *Performance of pile-up mitigation techniques for jets in pp collisions at $\sqrt{s} = 8$ TeV using the ATLAS detector*, *Eur. Phys. J. C* **76** (2016) 581, arXiv: [1510.03823 \[hep-ex\]](#) (cit. on p. 4).
- [17] ATLAS Collaboration, *Luminosity determination in pp collisions at $\sqrt{s} = 13$ TeV using the ATLAS detector at the LHC*, ATLAS-CONF-2019-021, 2019, URL: <https://cds.cern.ch/record/2677054> (cit. on p. 5).
- [18] G. Avoni et al., *The new LUCID-2 detector for luminosity measurement and monitoring in ATLAS*, *JINST* **13** (2018) P07017 (cit. on p. 5).
- [19] K. Hamilton, P. Nason, and G. Zanderighi, *MINLO: Multi-Scale Improved NLO*, *JHEP* **10** (2012) 155, arXiv: [1206.3572 \[hep-ph\]](#) (cit. on pp. 5, 6).
- [20] J. M. Campbell et al., *NLO Higgs Boson Production Plus One and Two Jets Using the POWHEG BOX, MadGraph4 and MCFM*, *JHEP* **07** (2012) 092, arXiv: [1202.5475 \[hep-ph\]](#) (cit. on pp. 5, 6).
- [21] K. Hamilton, P. Nason, C. Oleari, and G. Zanderighi, *Merging H/W/Z + 0 and 1 jet at NLO with no merging scale: a path to parton shower + NNLO matching*, *JHEP* **05** (2013) 082, arXiv: [1212.4504 \[hep-ph\]](#) (cit. on pp. 5, 6).
- [22] S. Alioli, P. Nason, C. Oleari, and E. Re, *A general framework for implementing NLO calculations in shower Monte Carlo programs: the POWHEG BOX*, *JHEP* **06** (2010) 043, arXiv: [1002.2581 \[hep-ph\]](#) (cit. on pp. 5, 6).
- [23] P. Nason, *A New method for combining NLO QCD with shower Monte Carlo algorithms*, *JHEP* **11** (2004) 040, arXiv: [hep-ph/0409146](#) (cit. on pp. 5, 6).
- [24] S. Frixione, P. Nason, and C. Oleari, *Matching NLO QCD computations with Parton Shower simulations: the POWHEG method*, *JHEP* **11** (2007) 070, arXiv: [0709.2092 \[hep-ph\]](#) (cit. on pp. 5, 6).
- [25] K. Hamilton, P. Nason, and G. Zanderighi, *Finite quark-mass effects in the NNLOPS POWHEG+MiNLO Higgs generator*, *JHEP* **05** (2015) 140, arXiv: [1501.04637 \[hep-ph\]](#) (cit. on p. 5).
- [26] A. Djouadi, J. Kalinowski, and M. Spira, *HDECAY: A program for Higgs boson decays in the Standard Model and its supersymmetric extension*, *Comput. Phys. Commun.* **108** (1998) 56, arXiv: [hep-ph/9704448](#) (cit. on p. 5).
- [27] M. Spira, *QCD Effects in Higgs physics*, *Fortsch. Phys.* **46** (1998) 203, arXiv: [hep-ph/9705337](#) (cit. on p. 5).
- [28] A. Djouadi, M. M. Mühlleitner, and M. Spira, *Decays of supersymmetric particles: The Program SUSY-HIT (SUSpect-SdecaY-Hdecay-InTeface)*, *Acta Phys. Polon. B* **38** (2007) 635, arXiv: [hep-ph/0609292](#) (cit. on p. 5).
- [29] A. Bredenstein, A. Denner, S. Dittmaier, and M. M. Weber, *Radiative corrections to the semileptonic and hadronic Higgs-boson decays $H \rightarrow WW/ZZ \rightarrow 4$ fermions*, *JHEP* **02** (2007) 080, arXiv: [hep-ph/0611234](#) (cit. on p. 5).

- [30] A. Bredenstein, A. Denner, S. Dittmaier, and M. M. Weber,
Precise predictions for the Higgs-boson decay $H \rightarrow WW/ZZ \rightarrow 4$ leptons,
Phys. Rev. D **74** (2006) 013004, arXiv: [hep-ph/0604011 \[hep-ph\]](#) (cit. on p. 5).
- [31] A. Bredenstein, A. Denner, S. Dittmaier, and M. M. Weber,
Precision calculations for the Higgs-boson decay $H \rightarrow ZZ/WW \rightarrow 4$ leptons,
Nucl. Phys. Proc. Suppl. **160** (2006) 131, arXiv: [hep-ph/0607060 \[hep-ph\]](#) (cit. on p. 5).
- [32] K. Becker et al., *Precise predictions for boosted Higgs production*, (2020),
arXiv: [2005.07762 \[hep-ph\]](#) (cit. on pp. 5, 6, 10, 17).
- [33] U. Blumenschein et al., “Pushing the precision frontier at the LHC with V+jets,” 2018,
arXiv: [1802.02100 \[hep-ex\]](#) (cit. on p. 5).
- [34] A. Gehrmann-De Ridder, T. Gehrmann, E. W. N. Glover, A. Huss, and T. A. Morgan,
Precise QCD predictions for the production of a Z boson in association with a hadronic jet,
Phys. Rev. Lett. **117** (2016) 022001, arXiv: [1507.02850 \[hep-ph\]](#) (cit. on pp. 5, 6).
- [35] A. Gehrmann-De Ridder, T. Gehrmann, E. W. N. Glover, A. Huss, and T. A. Morgan,
The NNLO QCD corrections to Z boson production at large transverse momentum,
JHEP **07** (2016) 133, arXiv: [1605.04295 \[hep-ph\]](#), We thank Nigel Glover and Alexander Huss
for providing $\sqrt{s} = 13$ TeV k-factors for the analysis fiducial volume. (Cit. on pp. 5, 6).
- [36] S. Frixione, P. Nason, and G. Ridolfi,
A Positive-weight next-to-leading-order Monte Carlo for heavy flavour hadroproduction,
JHEP **09** (2007) 126, arXiv: [0707.3088 \[hep-ph\]](#) (cit. on pp. 5, 6).
- [37] E. Re,
Single-top Wt-channel production matched with parton showers using the POWHEG method,
Eur. Phys. J. C **71** (2011) 1547, arXiv: [1009.2450 \[hep-ph\]](#) (cit. on pp. 5, 6).
- [38] R. Frederix, E. Re, and P. Torrielli,
Single-top t-channel hadroproduction in the four-flavour scheme with POWHEG and aMC@NLO,
JHEP **09** (2012) 130, arXiv: [1207.5391 \[hep-ph\]](#) (cit. on pp. 5, 6).
- [39] S. Alioli, P. Nason, C. Oleari, and E. Re,
NLO single-top production matched with shower in POWHEG: s- and t-channel contributions,
JHEP **09** (2009) 111, arXiv: [0907.4076 \[hep-ph\]](#) (cit. on pp. 5, 6),
Erratum: *JHEP* **02** (2010) 011.
- [40] S. Frixione, E. Laenen, P. Motylinski, C. White, and B. R. Webber,
Single-top hadroproduction in association with a W boson, *JHEP* **07** (2008) 029,
arXiv: [0805.3067 \[hep-ph\]](#) (cit. on p. 5).
- [41] T. Sjöstrand et al., *An introduction to PYTHIA 8.2*, *Comput. Phys. Commun.* **191** (2015) 159,
arXiv: [1410.3012 \[hep-ph\]](#) (cit. on pp. 5, 6).
- [42] ATLAS Collaboration, *The ATLAS Simulation Infrastructure*, *Eur. Phys. J. C* **70** (2010) 823,
arXiv: [1005.4568 \[physics.ins-det\]](#) (cit. on p. 5).
- [43] S. Agostinelli et al., *GEANT4 – a simulation toolkit*, *Nucl. Instrum. Meth. A* **506** (2003) 250
(cit. on p. 5).
- [44] R. D. Ball et al., *Parton distributions with LHC data*, *Nucl. Phys. B* **867** (2013) 244,
arXiv: [1207.1303 \[hep-ph\]](#) (cit. on pp. 5, 6).

- [45] ATLAS Collaboration, *The Pythia 8 A3 tune description of ATLAS minimum bias and inelastic measurements incorporating the Donnachie–Landshoff diffractive model*, ATL-PHYS-PUB-2016-017, 2016, URL: <https://cds.cern.ch/record/2206965> (cit. on p. 5).
- [46] D. J. Lange, *The EvtGen particle decay simulation package*, Nucl. Instrum. Meth. A **462** (2001) 152 (cit. on p. 5).
- [47] ATLAS Collaboration, *ATLAS simulation of boson plus jets processes in Run 2*, ATL-PHYS-PUB-2017-006, 2017, URL: <https://cds.cern.ch/record/2261937> (cit. on p. 5).
- [48] ATLAS Collaboration, *Studies on top-quark Monte Carlo modelling for Top2016*, ATL-PHYS-PUB-2016-020, 2016, URL: <https://cds.cern.ch/record/2216168> (cit. on p. 5).
- [49] ATLAS Collaboration, *Studies on top-quark Monte Carlo modelling with Sherpa and MG5_aMC@NLO*, ATL-PHYS-PUB-2017-007, 2017, URL: <https://cds.cern.ch/record/2261938> (cit. on p. 5).
- [50] ATLAS Collaboration, *Improvements in $t\bar{t}$ modelling using NLO+PS Monte Carlo generators for Run 2*, ATL-PHYS-PUB-2018-009, 2018, URL: <https://cds.cern.ch/record/2630327> (cit. on p. 5).
- [51] ATLAS Collaboration, *Multijet simulation for 13 TeV ATLAS Analyses*, ATL-PHYS-PUB-2019-017, 2019, URL: <https://cds.cern.ch/record/2672252> (cit. on p. 5).
- [52] A. Denner, S. Dittmaier, S. Kallweit, and A. Muck, *Electroweak corrections to Higgs-strahlung off W/Z bosons at the Tevatron and the LHC with HAWK*, JHEP **03** (2012) 075, arXiv: 1112.5142 [hep-ph] (cit. on p. 6).
- [53] A. Denner, S. Dittmaier, S. Kallweit, and A. Mück, *HAWK 2.0: A Monte Carlo program for Higgs production in vector-boson fusion and Higgs strahlung at hadron colliders*, Comput. Phys. Commun. **195** (2015) 161, arXiv: 1412.5390 [hep-ph] (cit. on p. 6).
- [54] F. Buccioni et al., *OpenLoops 2*, Eur. Phys. J. C **79** (2019) 866, arXiv: 1907.13071 [hep-ph] (cit. on p. 6).
- [55] F. Cascioli, P. Maierhöfer, and S. Pozzorini, *Scattering Amplitudes with Open Loops*, Phys. Rev. Lett. **108** (2012) 111601, arXiv: 1111.5206 [hep-ph] (cit. on p. 6).
- [56] A. Denner, S. Dittmaier, and L. Hofer, *COLLIER: A fortran-based complex one-loop library in extended regularizations*, Comput. Phys. Commun. **212** (2017) 220, arXiv: 1604.06792 [hep-ph] (cit. on p. 6).
- [57] R. D. Ball et al., *Parton distributions for the LHC run II*, JHEP **04** (2015) 040, arXiv: 1410.8849 [hep-ph] (cit. on p. 6).
- [58] ATLAS Collaboration, *Measurement of the Z/γ^* boson transverse momentum distribution in pp collisions at $\sqrt{s} = 7$ TeV with the ATLAS detector*, JHEP **09** (2014) 145, arXiv: 1406.3660 [hep-ex] (cit. on p. 6).

- [59] P. Nason and C. Oleari,
NLO Higgs boson production via vector-boson fusion matched with shower in POWHEG,
JHEP **02** (2010) 037, arXiv: [0911.5299 \[hep-ph\]](#) (cit. on p. 6).
- [60] G. Cullen et al., *Automated One-Loop Calculations with GoSam*, *Eur. Phys. J. C* **72** (2012) 1889,
 arXiv: [1111.2034 \[hep-ph\]](#) (cit. on p. 6).
- [61] G. Luisoni, P. Nason, C. Oleari, and F. Tramontano, *$HW^\pm/HZ + 0$ and 1 jet at NLO with the POWHEG BOX interfaced to GoSam and their merging within MiNLO*, *JHEP* **10** (2013) 083,
 arXiv: [1306.2542 \[hep-ph\]](#) (cit. on p. 6).
- [62] H. B. Hartanto, B. Jäger, L. Reina, and D. Wackerroth,
Higgs boson production in association with top quarks in the POWHEG BOX,
Phys. Rev. D **91** (2015) 094003, arXiv: [1501.04498 \[hep-ph\]](#) (cit. on p. 6).
- [63] T. Gleisberg et al., *Event generation with SHERPA 1.1*, *JHEP* **02** (2009) 007,
 arXiv: [0811.4622 \[hep-ph\]](#) (cit. on p. 6).
- [64] T. Gleisberg and S. Höche, *Comix, a new matrix element generator*, *JHEP* **12** (2008) 039,
 arXiv: [0808.3674 \[hep-ph\]](#) (cit. on p. 6).
- [65] S. Schumann and F. Krauss,
A parton shower algorithm based on Catani–Seymour dipole factorisation, *JHEP* **03** (2008) 038,
 arXiv: [0709.1027 \[hep-ph\]](#) (cit. on p. 6).
- [66] S. Höche, F. Krauss, M. Schönherr, and F. Siegert,
QCD matrix elements + parton showers. The NLO case, *JHEP* **04** (2013) 027,
 arXiv: [1207.5030 \[hep-ph\]](#) (cit. on p. 6).
- [67] S. Catani, L. Cieri, G. Ferrera, D. de Florian, and M. Grazzini,
Vector boson production at hadron colliders: a fully exclusive QCD calculation at NNLO,
Phys. Rev. Lett. **103** (2009) 082001, arXiv: [0903.2120 \[hep-ph\]](#) (cit. on p. 6).
- [68] S. Kallweit, J. M. Lindert, P. Maierhöfer, S. Pozzorini, and M. Schönherr,
NLO electroweak automation and precise predictions for W +multijet production at the LHC,
JHEP **04** (2015) 012, arXiv: [1412.5157 \[hep-ph\]](#) (cit. on p. 6).
- [69] B. Biedermann et al., *Automation of NLO QCD and EW corrections with Sherpa and Recola*,
Eur. Phys. J. C **77** (2017) 492, arXiv: [1704.05783 \[hep-ph\]](#) (cit. on p. 6).
- [70] ATLAS Collaboration, *ATLAS Pythia 8 tunes to 7 TeV data*, ATL-PHYS-PUB-2014-021, 2014,
 URL: <https://cds.cern.ch/record/1966419> (cit. on p. 6).
- [71] M. Czakon and A. Mitov,
Top++: A program for the calculation of the top-pair cross-section at hadron colliders,
Comput. Phys. Commun. **185** (2014) 2930, arXiv: [1112.5675 \[hep-ph\]](#) (cit. on p. 6).
- [72] ATLAS Collaboration,
Early Inner Detector Tracking Performance in the 2015 Data at $\sqrt{s} = 13$ TeV,
 ATL-PHYS-PUB-2015-051, 2015, URL: <https://cds.cern.ch/record/2110140>
 (cit. on p. 6).
- [73] ATLAS Collaboration, *Reconstruction of primary vertices at the ATLAS experiment in Run 1 proton–proton collisions at the LHC*, *Eur. Phys. J. C* **77** (2017) 332,
 arXiv: [1611.10235 \[hep-ex\]](#) (cit. on p. 6).

- [74] W. Lampl et al., *Calorimeter Clustering Algorithms: Description and Performance*, ATL-LARG-PUB-2008-002, 2008, URL: <https://cds.cern.ch/record/1099735> (cit. on p. 6).
- [75] ATLAS Collaboration, *Topological cell clustering in the ATLAS calorimeters and its performance in LHC Run 1*, *Eur. Phys. J. C* **77** (2017) 490, arXiv: [1603.02934](https://arxiv.org/abs/1603.02934) [hep-ex] (cit. on p. 6).
- [76] ATLAS Collaboration, *Selection of jets produced in 13 TeV proton–proton collisions with the ATLAS detector*, ATLAS-CONF-2015-029, 2015, URL: <https://cds.cern.ch/record/2037702> (cit. on p. 6).
- [77] D. Krohn, J. Thaler, and L.-T. Wang, *Jet trimming*, *Journal of High Energy Physics* **2010** (2010), ISSN: 1029-8479, URL: [http://dx.doi.org/10.1007/JHEP02\(2010\)084](http://dx.doi.org/10.1007/JHEP02(2010)084) (cit. on p. 6).
- [78] ATLAS Collaboration, *In situ calibration of large-radius jet energy and mass in 13 TeV proton–proton collisions with the ATLAS detector*, *Eur. Phys. J. C* **79** (2019) 135, arXiv: [1807.09477](https://arxiv.org/abs/1807.09477) [hep-ex] (cit. on pp. 6, 7).
- [79] D. Krohn, J. Thaler, and L.-T. Wang, *Jets with Variable R*, *JHEP* **06** (2009) 059, arXiv: [0903.0392](https://arxiv.org/abs/0903.0392) [hep-ph] (cit. on p. 7).
- [80] ATLAS Collaboration, *Variable Radius, Exclusive- k_T , and Center-of-Mass Subjet Reconstruction for Higgs($\rightarrow b\bar{b}$) Tagging in ATLAS*, ATL-PHYS-PUB-2017-010, 2017, URL: <https://cds.cern.ch/record/2268678> (cit. on p. 7).
- [81] M. Cacciari, G. P. Salam, and G. Soyez, *The Catchment Area of Jets*, *JHEP* **04** (2008) 005, arXiv: [0802.1188](https://arxiv.org/abs/0802.1188) [hep-ph] (cit. on p. 7).
- [82] M. Cacciari and G. P. Salam, *Pileup subtraction using jet areas*, *Phys. Lett. B* **659** (2008) 119, arXiv: [0707.1378](https://arxiv.org/abs/0707.1378) [hep-ph] (cit. on p. 7).
- [83] ATLAS Collaboration, *ATLAS b -jet identification performance and efficiency measurement with $t\bar{t}$ events in pp collisions at $\sqrt{s} = 13$ TeV*, *Eur. Phys. J. C* **79** (2019) 970, arXiv: [1907.05120](https://arxiv.org/abs/1907.05120) [hep-ex] (cit. on pp. 7, 8).
- [84] ATLAS Collaboration, *Muon reconstruction performance of the ATLAS detector in proton–proton collision data at $\sqrt{s} = 13$ TeV*, *Eur. Phys. J. C* **76** (2016) 292, arXiv: [1603.05598](https://arxiv.org/abs/1603.05598) [hep-ex] (cit. on p. 7).
- [85] ATLAS Collaboration, *Jet mass and substructure of inclusive jets in $\sqrt{s} = 7$ TeV pp collisions with the ATLAS experiment*, *JHEP* **05** (2012) 128, arXiv: [1203.4606](https://arxiv.org/abs/1203.4606) [hep-ex] (cit. on p. 8).
- [86] ATLAS Collaboration, *Jet mass reconstruction with the ATLAS Detector in early Run 2 data*, ATLAS-CONF-2016-035, 2016, URL: <https://cds.cern.ch/record/2200211> (cit. on p. 8).
- [87] ATLAS Collaboration, *Measurement of b -tagging efficiency of c -jets in $t\bar{t}$ events using a likelihood approach with the ATLAS detector*, ATLAS-CONF-2018-001, 2018, URL: <https://cds.cern.ch/record/2306649> (cit. on p. 8).
- [88] ATLAS Collaboration, *Calibration of light-flavour b -jet mistagging rates using ATLAS proton–proton collision data at $\sqrt{s} = 13$ TeV*, ATLAS-CONF-2018-006, 2018, URL: <https://cds.cern.ch/record/2314418> (cit. on p. 8).
- [89] ATLAS Collaboration, *Optimisation and performance studies of the ATLAS b -tagging algorithms for the 2017-18 LHC run*, ATL-PHYS-PUB-2017-013, 2017, URL: <https://cds.cern.ch/record/2273281> (cit. on p. 9).

- [90] J. M. Lindert, K. Kudashkin, K. Melnikov, and C. Wever,
Higgs bosons with large transverse momentum at the LHC, *Phys. Lett. B* **782** (2018) 210,
 arXiv: [1801.08226 \[hep-ph\]](#) (cit. on p. 10).
- [91] J. Lindert et al., *Precise predictions for V +jets dark matter backgrounds*,
Eur. Phys. J. C **77** (2017) 829, arXiv: [1705.04664 \[hep-ph\]](#) (cit. on p. 11).
- [92] T. Sjöstrand, *Jet fragmentation of multiparton configurations in a string framework*,
Nucl. Phys. B **248** (1984) 469 (cit. on p. 11).
- [93] W. Verkerke and D. Kirkby, *The RooFit toolkit for data modeling*, 2003,
 arXiv: [physics/0306116 \[physics.data-an\]](#) (cit. on p. 16).
- [94] S. Hageboeck, “What the new RooFit can do for your analysis,”
40th International Conference on High Energy Physics, 2020,
 arXiv: [2012.02746 \[physics.data-an\]](#) (cit. on p. 16).
- [95] *RooBinSamplingPdf*,
 URL: <https://root.cern.ch/doc/master/classRooBinSamplingPdf.html>
 (cit. on p. 16).
- [96] T. Junk, *Confidence level computation for combining searches with small statistics*,
Nucl. Instrum. Meth. A **434** (1999) 435, arXiv: [hep-ex/9902006](#) (cit. on p. 16).
- [97] A. L. Read, *Presentation of search results: the CL_S technique*, *J. Phys. G* **28** (2002) 2693
 (cit. on p. 16).
- [98] R. J. Barlow and C. Beeston, *Fitting using finite Monte Carlo samples*,
Comput. Phys. Commun. **77** (1993) 219 (cit. on p. 16).
- [99] M. Grazzini, A. Ilnicka, and M. Spira,
Higgs boson production at large transverse momentum within the SMEFT: analytical results,
Eur. Phys. J. C **78** (2018) 808, arXiv: [1806.08832 \[hep-ph\]](#) (cit. on p. 18).
- [100] ATLAS Collaboration, *Measurements of Higgs Bosons Decaying to Bottom Quarks from Vector
 Boson Fusion Production with the ATLAS Experiment at $\sqrt{s} = 13$ TeV*, (2020),
 arXiv: [2011.08280 \[hep-ex\]](#) (cit. on p. 18).
- [101] ATLAS Collaboration, *Measurements of WH and ZH production in the $H \rightarrow b\bar{b}$ decay channel in
 pp collisions at 13 TeV with the ATLAS detector*, (2020), arXiv: [2007.02873 \[hep-ex\]](#)
 (cit. on p. 18).
- [102] ATLAS Collaboration,
*Measurement of the associated production of a Higgs boson decaying into b-quarks with a vector
 boson at high transverse momentum in pp collisions at $\sqrt{s} = 13$ TeV with the ATLAS detector*,
 (2020), arXiv: [2008.02508 \[hep-ex\]](#) (cit. on p. 18).
- [103] ATLAS Collaboration, *Measurements of top-quark pair differential and double-differential
 cross-sections in the ℓ +jets channel with pp collisions at $\sqrt{s} = 13$ TeV using the ATLAS detector*,
Eur. Phys. J. C **79** (2019) 1028, arXiv: [1908.07305 \[hep-ex\]](#) (cit. on pp. 19, 20, 23).